Solar Physics
DOI: 10.1007/•••••-•••-•••-••••-•

Flare Related Recurring Active Region Jets: Evidence for Very Hot Plasma

Sargam M. Mulay[1,2] · **Sarah Matthews**[3] · **Takahiro Hasegawa**[4,5] · **Giulio Del Zanna**[1] · **Helen Mason**[1] · **Toshifumi Shimizu**[5]

Abstract

We present a study of two active region jets (AR jets) associated with two C-class X-ray flares. The recurrent, homologous jets originated from the northern periphery of a sunspot. We confirmed the presence of flare like temperatures at the footpoints of these jets using spectroscopic observations of Fe XXIII (263.76 Å) and Fe XXIV (255.11 Å) emission lines. The emission measure loci method was used to obtain an isothermal temperature and the results show a decrease (17.7 to 13.6 MK) in the temperature during the decay phase of the C 3.0 flare. The electron number densities at the footpoints were found to range from 1.7×10^{10} to 2.0×10^{11} cm^{-3} using the Fe XIV line pair ratio. Nonthermal velocities were found to range from 34-100 km/s for Fe XXIV and 51-89 km/s for Fe XXIII. The plane-of-sky velocities were calculated to be **462±21** and **228±23 km/s** for the two jets using the ***Atmospheric Imaging Assembly*** (AIA) 171 Å channel. The AIA light curves of the jet footpoint regions confirmed the temporal and spatial correlation between both xray flares and the jet footpoint emission. The ***Gamma-ray Burst Monitor*** (GBM) also confirmed the presence of superhot

✉ S. M. Mulay
smm96@cam.ac.uk, sargam@iucaa.in

1 DAMTP, Centre for Mathematical Sciences, University of Cambridge, Wilberforce Road, Cambridge, CB3 0WA, UK

2 Inter-University Centre for Astronomy and Astrophysics (IUCAA), Post Bag-4, Ganeshkhind, Pune 411007, India

3 Department of Space and Climate Physics, Mullard Space Science Laboratory, University College London, UK

4 Department of Earth and Planetary Science, Graduate School of Science, The University of Tokyo, 7-3-1, Hongo, Bunkyo-ku, Tokyo 113-0033, Japan

5 Institute of Space and Astronautical Science, Japan Aerospace Exploration Agency, 3-1-1, Yoshinodai, Sagamihara, Kanagawa 229-8510, Japan

plasma of 27 (25) MK with nonthermal energy of 2.38×10^{26} (2.87×10^{27}) erg s^{-1} in the jet footpoint region during the rise (peak) phase of one of the flares. The temperatures of the jet footpoint regions obtained from EIS show very good agreement (within 20% uncertainty) with temperatures obtained from the ***Geostationary Environmental Operational Satellite*** (GOES) flux ratios. These results provide clear evidence for very hot plasma (>10 MK) at the footpoints of the flare-related jets, while confirming the heating and cooling of the plasma during the flares.

Keywords: Active Regions, Corona, Flares, Heating, Jets, Spectral Line

1. Introduction

The impulsive and collimated events which originate at the edges of active regions and/or sunspots are known as active region jets (AR jets). Numerous studies have been dedicated to understanding the relationship between AR jets and other phenomena such as micro-flares (Chae *et al.*, 1999; Chifor *et al.*, 2008), flares (Chen, Ip, and Innes, 2013; Krucker *et al.*, 2008), hard X-ray emission (Bain and Fletcher, 2009; Krucker *et al.*, 2011; Glesener, Krucker, and Lin, 2012), **Coronal Mass Ejections (CMEs) (Liu *et al.*, 2015; Panesar, Sterling, and Moore, 2016; Miao *et al.*, 2017; Sterling, Moore, and Panesar, 2018)**, type-III radio bursts (Kundu *et al.*, 1995; Raulin *et al.*, 1996; Klassen, Gómez-Herrero, and Heber, 2011; Innes, Cameron, and Solanki, 2011; Chandra *et al.*, 2015; Mulay *et al.*, 2016) and impulsive solar energetic particle events (Nitta *et al.*, 2006; Pick *et al.*, 2006; Nitta *et al.*, 2008; Wang, Pick, and Mason, 2006; Nitta *et al.*, 2015).

From imaging observations of AR jets, it has been found that different X-ray flares of all classes observed by the ***Geostationary Environmental Operational Satellite*** (GOES) including B-class (Chifor *et al.*, 2008), C-class (Zhang and Ji, 2014; Mulay *et al.*, 2016; Hong *et al.*, 2017) and M-class (Bain and Fletcher, 2009; Li *et al.*, 2015) are temporally associated with jets. Out of 20 AR jets studied in Mulay *et al.* (2016), three (five) jets were temporally associated with B-class (C-class) X-ray flares. The helical structure and **rotating** motion of EUV AR jets has been observed in many events (Mulay *et al.*, 2016) and their plane-of-sky velocities ranged from 80-500 km/s. Li *et al.* (2015) reported flux emergence whereas Zhang and Ji (2014) and Chifor *et al.* (2008) reported magnetic flux cancellation as the cause of the flare related AR jet events.

The temporal and spatial correlation of the jet activity with hard X-ray emission has been studied using the ***Reuven Ramaty High Energy Solar Spectroscopic Imager*** (RHESSI; Lin *et al.*, 2002). The first observation of hard X-ray emission formed in a coronal jet was reported by Bain and Fletcher (2009). The authors measured apparent velocities of 500 km/s. The RHESSI imaging data showed the presence of 30-50 keV hard X-ray sources at the footpoint region and a jet temperature of 28 MK was measured from the spectroscopic data. Krucker *et al.* (2011) reported observation of three hard X-ray sources; two at the footpoint and one along the jet spire. The thermal sources (<10 keV) were

found to be associated with the top of the loop which was associated with a jet footpoint region. Glesener, Krucker, and Lin (2012) observed double coronal hard X-ray sources in the pre-impulsive phase and found temperatures of 13, 24 and 22 MK during the evolution of the jet whereas Christe, Krucker, and Lin (2008) and Bain and Fletcher (2009) reported the presence of superhot plasma of 26 and 28 MK respectively.

The temperature structure of AR jets has been studied using imaging observations from the ***Atmospheric Imaging Assembly*** **(AIA)** (Chen, Ip, and Innes, 2013; Mulay *et al.*, 2016; Mulay, Del Zanna, and Mason, 2017a), spectroscopic observation from the ***EUV Imaging Spectrometer*** (EIS) on board Hinode (Madjarska, 2011; Mulay, Del Zanna, and Mason, 2017b), the ***Interface Region Imaging Spectrograph*** (IRIS) (Mulay, Del Zanna, and Mason, 2017a) and RHESSI (Glesener, Krucker, and Lin, 2012). Making use of AIA observations in the DEM analysis, Chen, Ip, and Innes (2013) reported a temperature of 7 MK whereas Liu *et al.* (2016) reported even higher temperature of 16 MK in a jet and suggested the possibility of nanoflares occurring at the footpoint region of the jet. Mulay, Del Zanna, and Mason (2017b) pointed out that there is always an uncertainty associated with temperature estimation using only imaging observations (such as AIA) in the DEM analysis. This is due to the lack of constraints on the low and high temperature part of the DEM solution. Madjarska (2011) studied the temperature structure of a micro-flare related coronal hole jet (CH jet) using the EIS instrument and found weak emission from the Fe XXIII line at a temperature of 12 MK at the footpoint of a jet. We also analysed the same observation but did not find the evidence convincing. All the above studies individually investigated the temperature distribution of AR jets using various observations. But none of the studies confirmed the hot emission simultaneously using imaging and spectroscopic observations of AR jets.

In this paper, we have studied homologous and recurring AR jet events which were associated with C-class X-ray flares. We have carried out the first thorough investigation of hot plasma (>10 MK) observed in AR jets using GOES, spectroscopic observations from EIS (using Fe XXIII (263.76 Å) and Fe XXIV (192.02, 255.11 Å) emission lines), EUV imaging data from AIA, X-ray imaging data from RHESSI and spectroscopic data from the ***FERMI Gamma-ray Burst Monitor*** (GBM).

The paper is organised as follows. In section 2, we present the AR jet observations and data analysis. In section 3, we summarize our results and compare them with results available in the literature. **This project has been funded through the award of the Daiwa-Adrian Prize through the Daiwa Anglo-Japanese foundation.**

2. Observations and Data Analysis

2.1. UV/EUV Imaging Observations from AIA

High-resolution (0.6″ per pixel), high-cadence (12 sec) full disk data from the AIA instrument (Lemen *et al.*, 2012) on board Solar Dynamic Observatory

(SDO; Pesnell, Thompson, and Chamberlin, 2012) were obtained for a recurrent AR jet observed on **9 March 2015** during 00:00 - 01:30 UT. The data (level 1.0) was downloaded using the Virtual Solar Observatory[1] (VSO) and prepared for a scientific analysis (level 1.5) using the standard AIA software package (`aia_prep.pro`) available in the SolarSoftWare[2] (SSW; Freeland and Handy, 1998) libraries. The intensities in the UV and EUV channels were normalized by the exposure time.

Different AIA channels are dominated by a range of EUV emission lines which originate at different temperatures. This leads to the multithermal nature of the AIA channels (O'Dwyer *et al.*, 2010; Del Zanna, O'Dwyer, and Mason, 2011; Del Zanna, 2013a; Del Zanna *et al.*, 2015) : 94 Å (Fe X, Fe XIV, Fe XVIII), 131 Å (Fe VIII, Fe XXI), 171 Å (Fe IX), 193 Å (Fe XII, Ca XVII, Fe XXIV), 211 Å (Fe XIV), 304 Å (He II 303.8 Å, emission from Si XI 303.3 Å line may contribute up to 20% to the total intensity in the channel in case of active region observations), 335 Å (Fe XVI), 1600 Å (C IV + continuum) and 1700 Å (continuum). The EUV AIA channels were coaligned carefully by examining the position of a sunspot in the AIA 1600 Å channel.

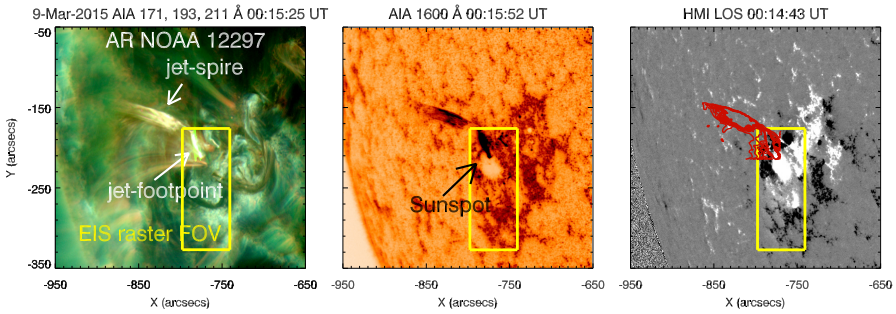

Figure 1. Left panel : a composite image of the active region NOAA 12297 (S17 E39) observed on **9 March 2015** at 00:15:25 UT. The image is created by combining the AIA 171 (red), 193 (green), 211 Å (blue) channels. The spire and footpoint regions of the jet are shown by white arrows. Middle panel : AIA 1600 Å image (reverse colour) at 00:15:52 UT. The black arrow indicates a sunspot which was associated with the active region. Right panel : the line-of-sight HMI photospheric magnetogram at 00:14:43 UT. The black and white regions represent the negative (-200 G) and positive (200 G) magnetic fields respectively. The red overplotted contours represent the jet observed at 00:15:25 UT in the AIA 171 Å channel. The yellow boxes in the images represent the EIS raster field-of-view. The footpoint region of the jet was well captured in a number of EIS rasters during the recurring jet activity.

The activity of NOAA 12297 (S17 E39) was examined in the different AIA channels. The active region was associated with a positive polarity sunspot (Hale class $\beta\gamma\delta$ configuration[3]) on its eastern periphery. The active region was producing homologous recurrent jets from the eastern edge continuously for many hours on both days - **8 and 9 March 2015** (see online movie1.mp4).

[1]https://sdac.virtualsolar.org/cgi/search

[2]http://www.lmsal.com/solarsoft/ssw_whatitis.html

[3]https://www.solarmonitor.org/?date=20150309

Using near-simultaneous images in the three AIA channels, we created a composite image of the active region during the recurrent jet activity. The red, green and blue colours in fig. 1 (left panel) correspond to the AIA 171, 193 and 211 Å channels respectively. The jet's spire and footpoint regions are shown by white arrows. The sunspot associated with active region is shown by black arrow in AIA 1600 Å image (middle panel). The yellow boxes represent the field-of-view observed by the EIS raster which covered the footpoint region of the recurrent jet. A small loop-like structure at the footpoint region was seen (associated with an umbral-penumbral region of a sunspot), which is similar to that observed in the AR jet observation discussed in Mulay *et al.* (2016) (Jet 1 - August 2, 2010).

We studied the AIA images during 00:00 - 01:30 UT and observed a couple of homologous dynamic jets. We have analysed two AR jets in this paper which were observed at 00:14 and 01:14 UT and referred to as jet 1 (see fig. 2) and 2 (see fig. 3) respectively. The activity of jet 1 started with a small brightening at the footpoint region which was observed at 00:13:52 UT in the AIA 1600 Å channel. The jet spire originated from the footpoint region at 00:14 UT and started its journey along the curved field lines associated with the active region. The multi-threaded spire was seen to be traveling until 00:16:50 UT. The spire-plasma started to fade away and eventually disappeared at 00:23 UT.

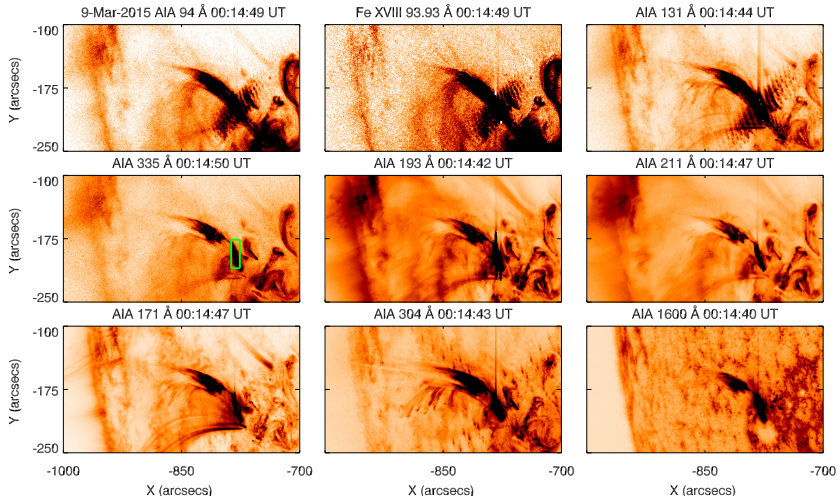

Figure 2. The images of AR jet 1 at 00:14 UT in all AIA channels (reverse colour images). The images confirmed the multithermal nature of the plasma emission in the spire and footpoint regions of a jet (see online movie1.mp4). The footpoint region was observed to be associated with an umbral-penumbral region of the sunspot (see AIA 1600 Å image). The Fe XVIII 93.93 Å emission (first row middle panel) is derived from the AIA 94 Å channel. A small green boxed region in the AIA 335 Å image was used to obtain AIA light curves (see fig. 4, bottom panel).

A similar scenario was observed during the evolution of jet 2. The activity of jet 2 started with a brightening at the footpoint which was observed at 01:08:40 UT. The jet spire followed the curved field lines, but some jet-plasma was also seen to be deviating from this path and started to flow along the closed

field lines which were present on the east side of the active region. Eventually, the spire-plasma faded away in all AIA channels and disappeared at 00:24 UT.

Figures 2 and 3 show images of jet 1 and 2 at 00:14 and 01:14 UT respectively, in all AIA channels. The footpoint regions of the jets were clearly observed to be associated with an umbral-penumbral region of the sunspot in the AIA 1600 Å channel (bottom right). The AIA images confirmed the multithermal nature of the spire and footpoint regions of both jets. The images in the AIA 94, 131, 193 and 304 Å channels show saturation (diffraction pattern) at the footpoint region of both jets.

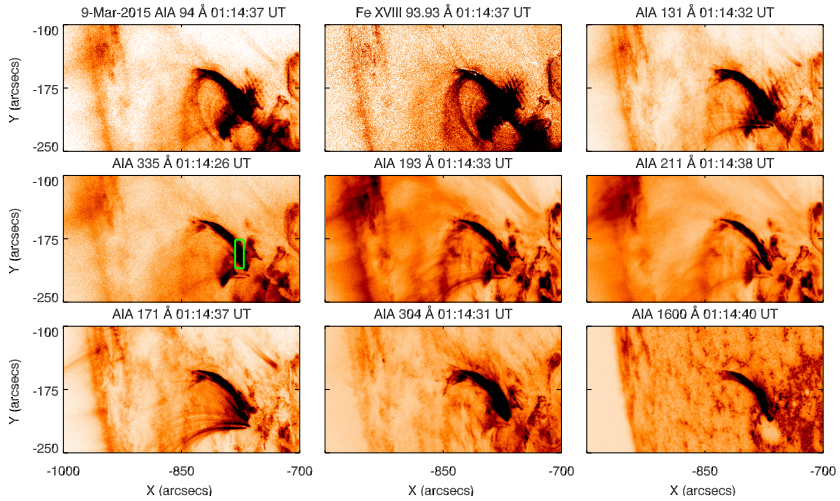

Figure 3. The images of the AR jet 2 at 01:14 UT in all AIA channels (reverse colour images). The images confirmed a multithermal plasma emission in the spire and footpoint region of the jet (see online movie1.mp4). The footpoint region was observed to be associated with an umbral-penumbral region of the sunspot (see AIA 1600 Å image). The Fe XVIII 93.93 Å emission (first row middle panel) is derived from the AIA 94 Å channel. A small green boxed region in the AIA 335 Å image was used to obtain AIA light curves (see fig. 5, bottom panel).

Using near simultaneous images in the AIA 94, 211 and 171 Å channels during the jet activity, we estimated Fe XVIII 93.932 Å emission using a semi-empirical formula, I (Fe XVIII) = I (94 Å) – (I (211 Å)/120) – (I (171 Å)/450) given by Del Zanna (2013b). A comparison of AIA 94 Å images with the derived Fe XVIII emission showed that the AIA 94 Å channel was dominated by Fe XVIII emission during the evolution of both jets. The cool and hot plasma components in the spire and footpoint regions of the jets are shown in AIA 304 Å (row 3, middle panel) and Fe XVIII images (row 1, middle panel) in figs. 2 and 3. The observations confirmed that there is a temporal and spatial correlation between hot and cool plasma components.

The X-ray activity during the evolution of the recurrent jet was examined using GOES-15 observations. The C 3.0 class X-ray flare started at 00:12 UT, peaked at about 00:14:30 UT and ended at 00:17 UT whereas; the C 1.8 class flare started at 01:07 UT, peaked at about 01:14:30 UT and ended at 01:17 UT.

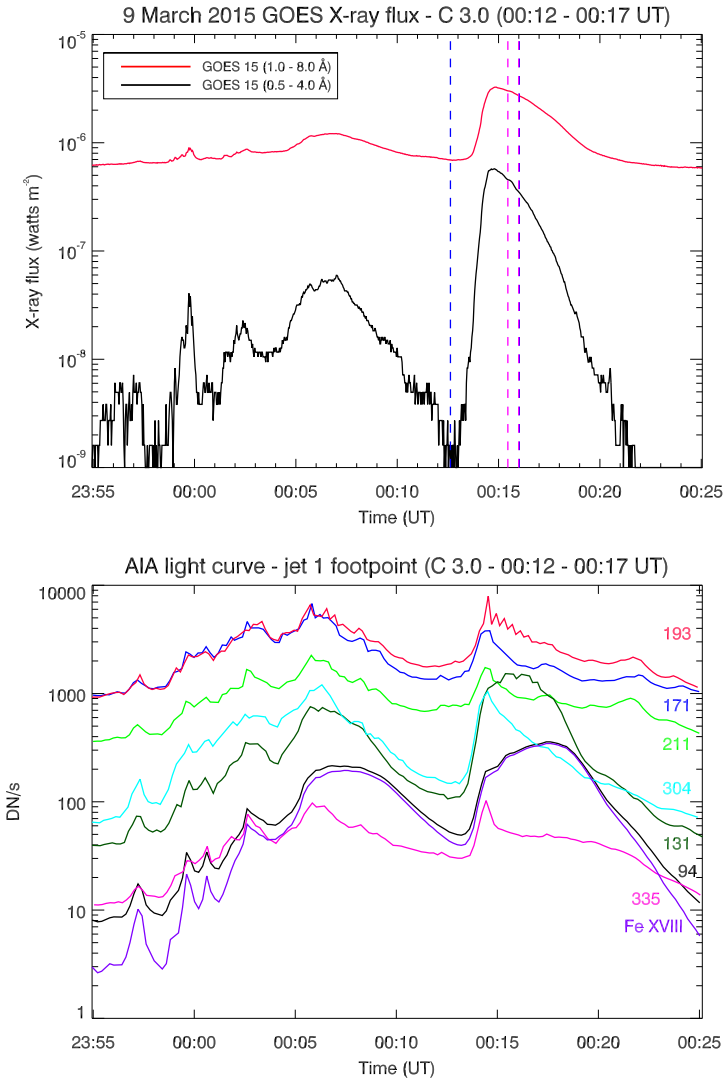

Figure 4. Top panel : the X-ray C 3.0 class flare observed on **9 March 2015** between 00:12 - 00:17 UT. The black and red curves show X-ray fluxes in the 0.5 - 4.0 Å and 1.0 - 8.0 Å channels of the GOES-15 respectively. The blue dashed lines indicate the start (00:12:33 UT) and end times (00:16:04 UT) of the EIS raster respectively, for AR jet 1. The pink lines indicate slit timings within the same raster (00:15:23 - 00:15:59 UT) where EIS observed emission from the footpoint region of jet 1. A small peak between 00:03 and 00:09 UT represents a C 1.1 X-ray flare. Bottom panel : the temporal evolution of the footpoint of AR jet 1 in all AIA channels. A small green boxed region shown in AIA 335 Å image in fig. 2 was used to obtain AIA light curves. The Fe XVIII 93.932 Å emission was estimated from the AIA 94 Å channel.

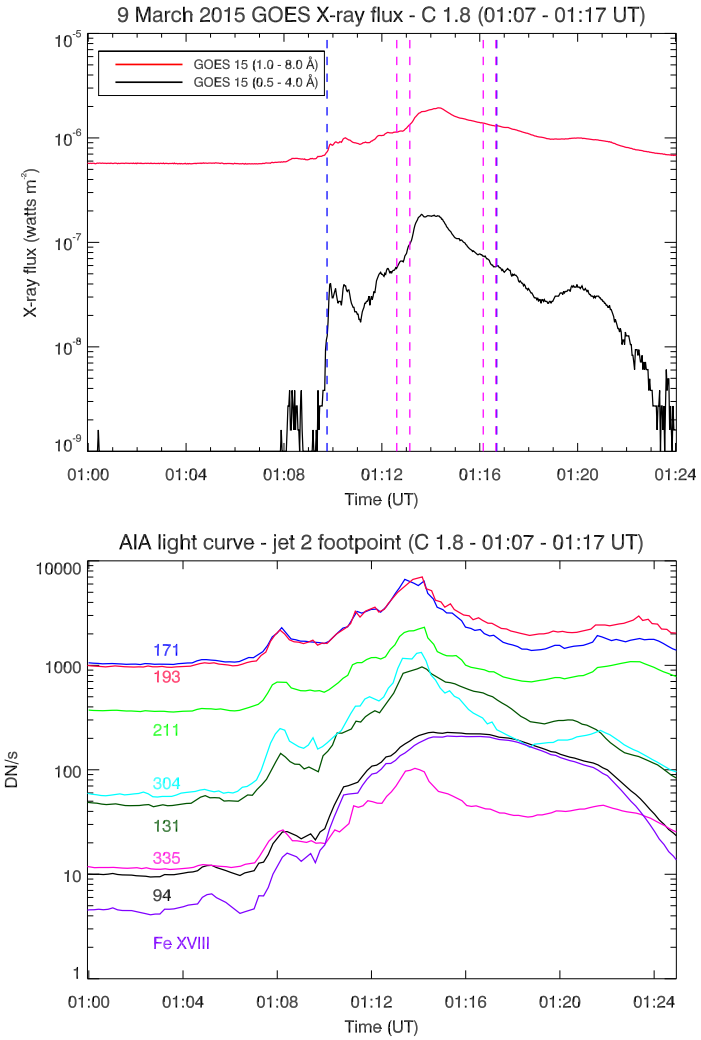

Figure 5. Top panel : the X-ray C 1.8 class flare observed on **9 March 2015** during 01:07 - 01:17 UT. The black and red curves show X-ray fluxes in the 0.5 - 4.0 Å and 1.0 - 8.0 Å channels of GOES-15 respectively. The blue dashed lines indicate the start time (01:09:41 UT) of the first raster and end time **(01:16:46 UT)** of the second raster respectively. The pink lines indicate slit timings within the first (01:12:31 - 01:13:03 UT) and second raster (01:16:05 - 01:16:37 UT) when the EIS raster captured emission from the footpoint region of jet 2. Bottom panel : the temporal evolution of the footpoint of the AR jet 2 in all AIA channels. A small green boxed region shown in AIA 335 Å image in fig. 3 was used to obtain AIA light curves. The Fe XVIII 93.932 Å emission was estimated from the AIA 94 Å channel.

The evolution of the X-ray fluxes during the flares is shown in figs. 4 and 5 (top panels) during the activity of AR jet 1 and 2 respectively. The black and red curves show X-ray fluxes obtained from the 0.5 - 4.0 Å and 1.0 - 8.0 Å channels of the GOES-15 satellite respectively. Jet 1 and 2 were found to be temporally associated with the X-ray C 3.0 and C 1.8 class flares respectively.

The activity of the footpoint region of both jets was examined in all AIA channels. A small green boxed regions in the AIA 335 Å channel of figs. 2 and 3 were used to obtain AIA light curves. Figures 4 and 5 (bottom panels) show AIA light curves obtained during the evolution of the footpoint region of jet 1 and 2 respectively. After a careful examination, it was found that the AIA light curves in all channels follow a similar pattern of activity as observed in the X-ray flares (see figs. 4 and 5, top panels). The observations showed that there is a temporal and spatial correlation between both flares and the emission from the footpoints. The results confirmed that both X-ray C-class flares originated at the footpoint regions of the jets.

Most of the images in the AIA 94 and 131 Å channels were saturated at the footpoint region during the peak and gradual decay phase of both flares. The light curves do not show sharp peaks as with the X-ray flares, rather the curves are broader during that time. The Fe XVIII 93.932 Å emission was estimated from the AIA 94 Å. The Fe XVIII light curve seems to follow the same pattern as the light curve obtained from the AIA 94 Å. This confirms that the AIA 94 Å was dominated by Fe XVIII 93.932 Å emission at the footpoint region during both flares. The AIA 131 Å channel was likely dominated by emission from Fe XXI 128.75 Å line during both flare-jet activity.

2.1.1. ***Plane-of-sky Velocities using AIA 171 Å images***

The plane-of-sky velocities for both AR jets were calculated using the AIA 171 Å channel (dominated by the Fe IX 171.07 Å line formed at log T [K] = 5.85 (0.7 MK)). Figure 6 shows AR jet 1 (top left panel) and 2 (bottom left panel) images in the AIA 171 Å channels.

The white overplotted lines along the jet spire were used to track the jet-front during the evolution. The time-distance plots (top and bottom right panels) were created. The near vertical features at 00:15 and 01:12 UT show signatures of AR jet 1 and 2 respectively. The **three** white dashed lines **were drawn along the threaded structure of the jet-spire and these lines were** used to measure the plane-of-sky velocities **(see Table 1)**. The **averaged** velocities were found to be **462±21** and **228±23 km/s** for jet 1 and 2 respectively. The vertical feature at 23:30 UT represents one of the recurrent jets which originated from the same footpoint region before the AR jet 1.

2.2. EUV Spectroscopic Observations from EIS

The EIS (Culhane *et al.*, 2007) on board the Hinode (Kosugi *et al.*, 2007) satellite was observing a small field-of-view ($59''\times152''$ shown as yellow boxes in fig. 1) of the active region NOAA 12297 (S17 E39) on 8 and **9 March 2015**. The *HH_Flare_raster_v6* study was running continuously for several hours to capture

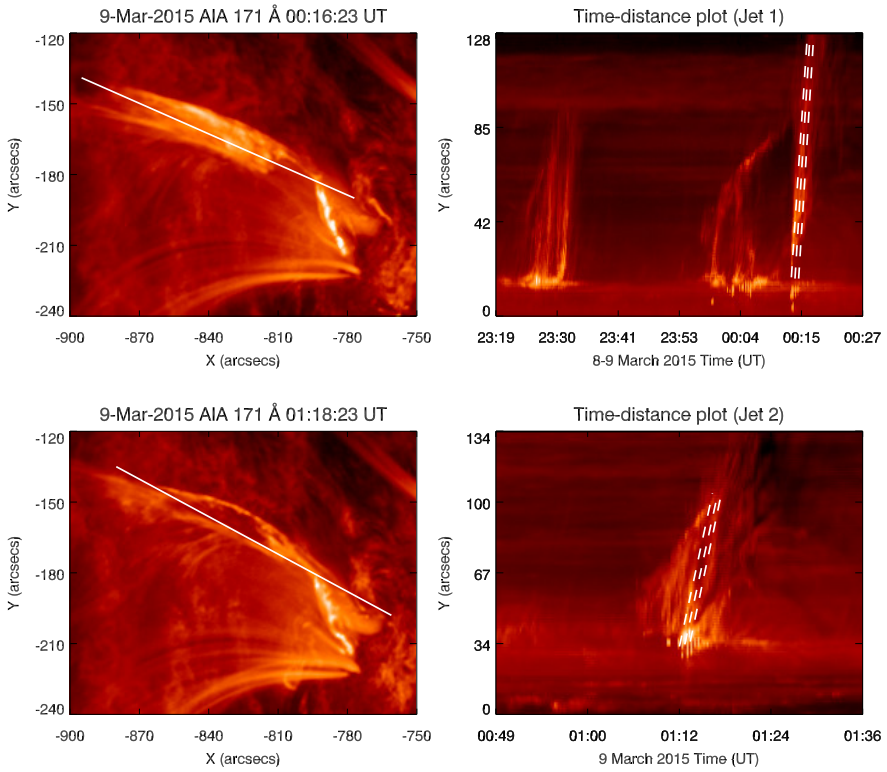

Figure 6. Left panel : The AIA 171 Å images of jet 1 at 00:16:23 UT (top panel) and jet 2 at 01:18:23 UT (bottom panel). The white overplotted lines represent artificial slits which were used to create time-distance plots. Right panel : Time distance plots for jet 1 (top panel) and jet 2 (bottom panel). The **three** white dashed lines along the jet-spire structure were used for the plane-of-sky velocity calculation. The velocities were found to be **462±21** and **228±23 km/s** for jet 1 and 2 respectively.

Table 1. Plane-of-sky velocities of the recurrent jet

Velocity (km/s)	Jet 1	Jet 2
Slit 1	448	223
Slit 2	486	209
Slit 3	452	253
Average Velocity	462±21	228±23

a flare. A total of 12 wavelength windows were used for this observation covering some high and low temperature lines in both short (SW: 166 - 212 Å) and long (LW: 245 - 291 Å) wavelength channels of the EIS instrument. A 2″**-wide** slit was moving in the Solar West-East direction (in the opposite direction to the Solar rotation) on the solar disk. The study used a sparse raster (3″ spacing between exposures). The raster covered 20 positions with 9 sec exposure time. Other details of the EIS observations and a list of the observed spectral lines are given in Tables 2 and 3 respectively.

Table 2. EIS observation details

EIS study details	
Observation date	**9 March 2015**
Study	Flare obs for AR near E-limb
Study acronym	HH_Flare_raster_v6
Raster start time (UT)	00:12:33
Raster end time (UT)	00:16:04
Raster type	scanning
Number of line windows	12
Number of exposures	20
Slit width	2″ (sparse raster)
Field-of-view	59″ × 152″
Raster cadence	3 min 31 sec
Exposure time (sec)	9.0
Pixel size in Solar-X	3.0″
Pixel size in Solar-Y	1.0″

The EIS data was downloaded from the Hinode Science Data Centre Europe[4] and converted to level 1 using the `eis_prep.pro` routine. The spectral lines were fitted with a single Gaussian profile at each pixel and intensities (DN) were obtained. The intensity images were created for each line. The intensities (DN) were converted to calibrated units (erg cm^{-2} s^{-1} sr^{-1}) using the radiometric calibration by Del Zanna (2013b). This calibration can be used for the EIS data which was observed before September 2012. For the data after September 2012, the calibration assumes that there is no degradation in the EIS channels and it calibrates data using the same degradation factor as that for September 2012.

EIS observed the active region during the impulsive, peak and decay phase of the C 3.0 class flare in a single raster (EIS raster start time - 00:12:33 UT and end time - 00:16:04 UT). The EIS raster captured emission from the footpoint region of AR jet 1 in four slit positions (slit number 17 - 20) during 00:15:23 - 00:15:55 UT i.e. during the decay phase of the flare. In Figure 4 (top panel), the blue lines show the raster start and end times and the pink dashed lines indicate

[4]http://sdc.uio.no/search/form

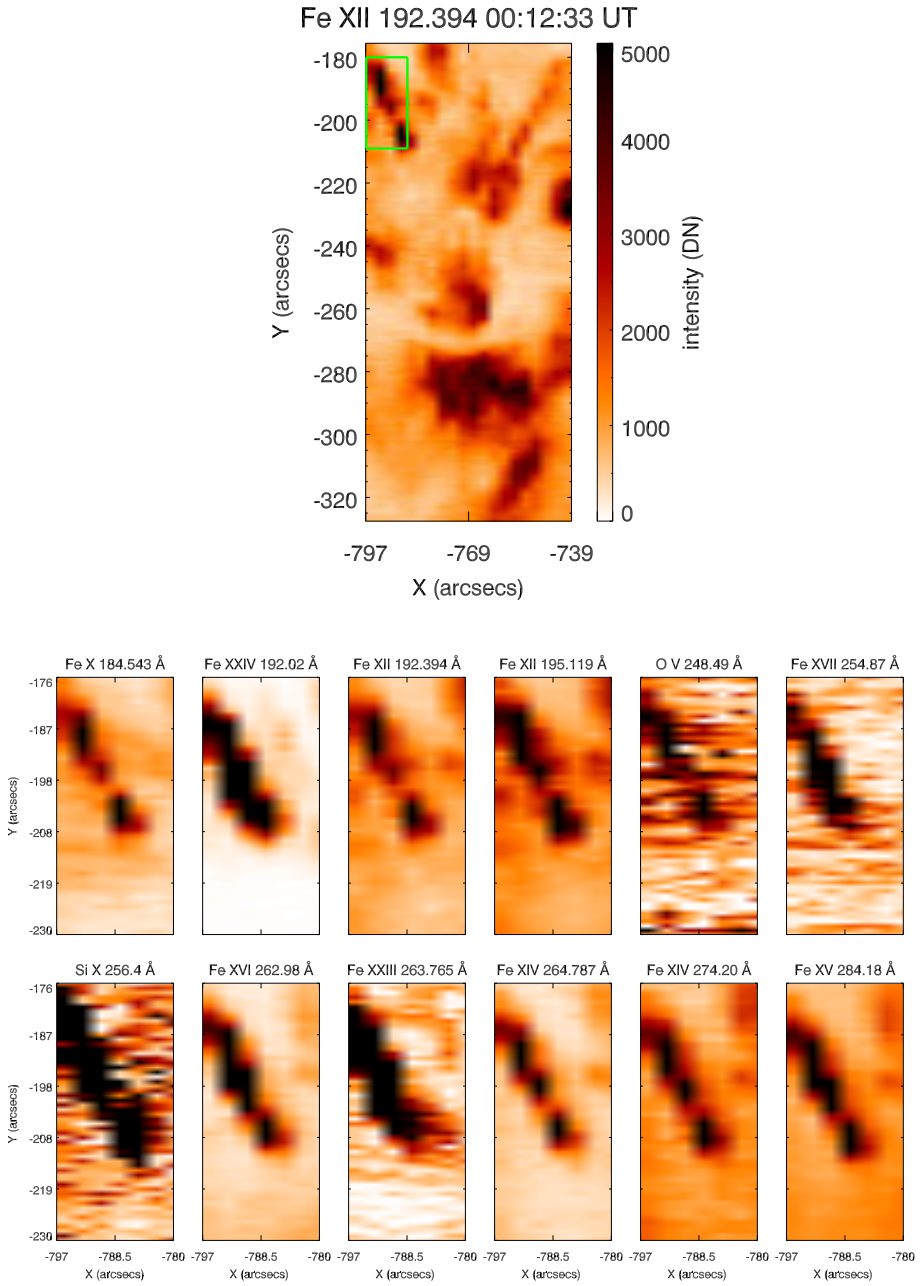

Figure 7. Top panel : EIS intensity image (reverse colours) in Fe XII (192.39 Å) created using the EIS raster observed at 00:12:33 UT. The green box indicates the emission observed from the footpoint region of jet 1 which covered four slit positions. Bottom panel : EIS intensity images (reverse colours) (zoomed view) of the footpoint region of jet 1.

Table 3. List of the EIS emission lines observed in this study

EIS observed lines	Wavelength λ (Å)	log T_{max} [K]
Fe X	184.54	6.1
Fe XXIV (bl)	192.02	7.25
Fe XII	192.39	6.2
Ca XVII (bl)	192.82	6.7
Fe XII (sbl)	195.12	6.2
O V	248.49	5.5
Fe XVII	254.87	6.8
Fe XXIV	255.11	7.25
Si X (bl)	256.40	6.1
Fe XVI	262.98	6.4
Fe XXIII	263.76	7.1
Fe XIV	264.79	6.2
Fe XIV (bl)	274.20	6.2
Fe XV	284.16	6.3

Notes. bl and sbl indicate blending and self-blending, respectively.

timings during which the raster captured emission from the footpoint region of AR jet 1.

Figure 7 (top panel) shows the EIS raster in Fe XII 192.39 Å line during the evolution of jet 1. The green box represents the region where the EIS raster (slit number 17 - 20) captured emission from the footpoint region of jet 1. A zoomed view of the footpoint region of jet 1 is shown in fig. 7 (bottom panel).

In the case of AR jet 2, two EIS rasters (raster 1 : 01:09:41 - 01:13:12 UT and raster 2 : 01:13:15 - 01:16:46 UT) observed emission during the impulsive, peak and decay phase of the X-ray C 1.8 class flare. Similar to jet 1 EIS observations, the footpoint region of jet 2 was also observed in four slit positions (slit number 17 - 20) in both rasters (raster 1 : 01:12:31 - 01:13:03 UT and raster 2 : 01:16:05 - 01:16:37 UT) during the impulsive and decay phase of the flare respectively. The pink dashed lines in fig. 5 indicate timings during which the raster captured emission from the footpoint region of AR jet 2.

2.2.1. Density Diagnostics using the Fe XIV Line Ratio

Currently, the EIS calibration is uncertain and we found some inconsistent densities using different line ratios. We measured electron number densities in the footpoint region of jets using density diagnostics from Fe XIV (264.79 and 274.20 Å) lines where the lines are close in wavelength. The electron number density in the footpoint regions of jet 1 and 2 was calculated using the CHIANTI v.8.0.2

atomic database (Dere *et al.*, 1997; Del Zanna *et al.*, 2015). Figure 8 (top panel) shows the theoretical line intensitv ratios for these Fe XIV lines.

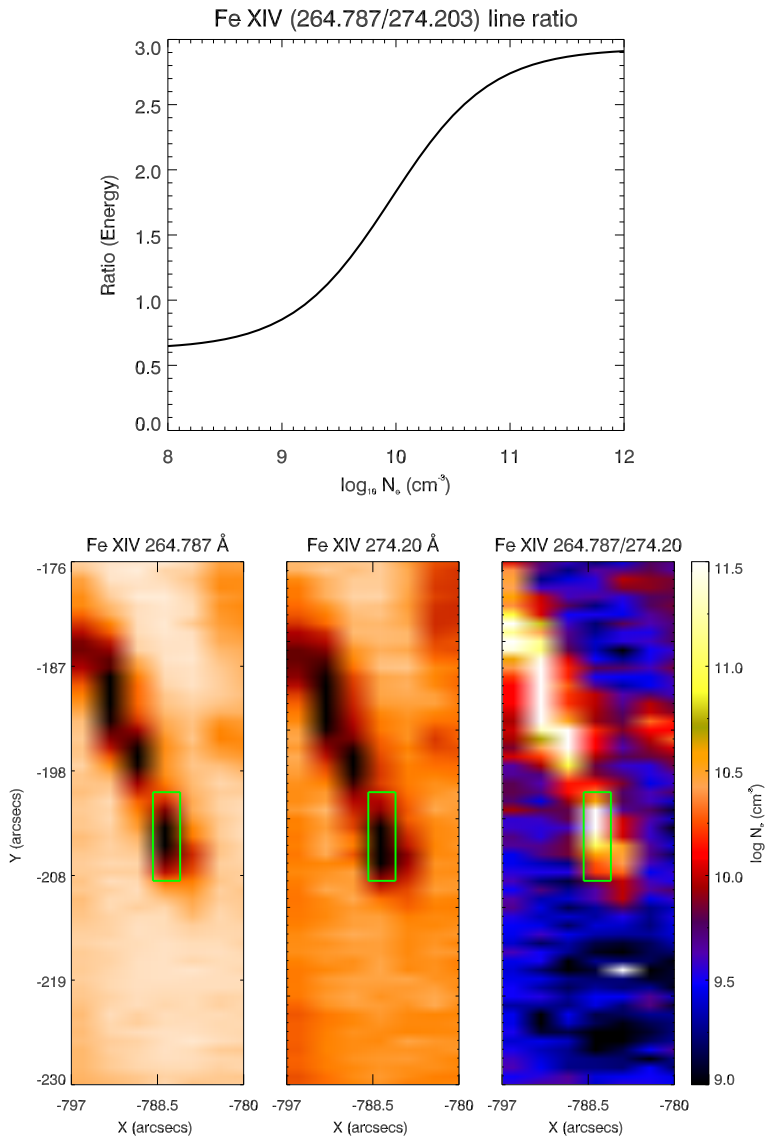

Figure 8. Top panel : the theoretical intensity ratio for Fe XIV (λ264.78/λ274.20) line pairs as a function of electron number density. Bottom panel : the Fe XIV intensity images (left and middle panel) and electron number density map (right panel) for jet 1. The green boxes show a region from slit 17 which was selected to calculate density in the the footpoint of jet 1. The electron number densities are in logarithmic scale in cm^{-3} units.

Table 4. Electron number densities obtained from Fe XIV line ratio density diagnostics

Event	Time (UT)	Y (pixel)	Fe XIV Density (N_e cm^{-3})
AR Jet 1 - Raster 1 - 00:12:33 - 00:16:04 UT			
slit 17	00:15:23	119:127	4.7×10^{10}
slit 18	00:15:33	123:133	2.7×10^{10}
slit 19	00:15:44	129:143	5.3×10^{10}
slit 20	00:15:55	140:148	4.6×10^{10}
AR Jet 2 - Raster 1 - 01:09:41 - 01:13:12 UT			
slit 17	01:12:31	121:130	2.6×10^{10}
slit 18	01:12:42	123:133	1.7×10^{10}
slit 19	01:12:52	127:140	2.0×10^{11}
slit 20	01:13:03	129:141	3.2×10^{10}
AR Jet 2 - Raster 2 - 01:13:15 - 01:16:46 UT			
slit 17	01:16:05	120:130	2.0×10^{10}
slit 18	01:16:15	125:135	2.1×10^{10}
slit 19	01:16:26	127:140	4.4×10^{10}
slit 20	01:16:37	133:148	4.1×10^{10}

The Fe XIV 264.79 Å line is unblended whereas Fe XIV 274.20 Å line is blended with the Si VII 274.175 Å. The contribution of the Si VII 274.175 Å can be estimated by using the other Si VII 275.35 Å line. But unfortunately, this study did not include the other Si VII line. So its contribution could not be included. Therefore, the densities measured here show lower limits. However, only a small contribution from Si VII to the Fe XIV line has been reported during the flares by Brosius (2013), Del Zanna *et al.* (2011) and Polito *et al.* (2016).

The densities obtained in the footpoint region of jet 1 and 2 using Fe XIV density diagnostics were found to be lower than the values obtained by Mulay, Del Zanna, and Mason (2017b) and Chifor *et al.* (2008) using Fe XII density diagnostics except for one slit position (slit 19 for Fe XIV for AR jet 2) where the densities show good agreement. The densities show good agreement with the values obtained by Mulay *et al.* (2016) which were lower limits to the densities.

2.2.2. ***Fe*** XXIII ***and Fe*** XXIV ***Line Profiles***

During the evolution of jet 1 and 2, the EIS raster observed emission from very hot plasma (>10 MK) from Fe XXIV (192.02, 255.11 Å) and Fe XXIII (263.76 Å) lines at the footpoint region of jets where the flares occurred. Figure 9 shows Fe XXIV 192.02 Å (left panel), Fe XXIV 255.11 Å (middle panel) and Fe XXIII 263.76 Å (right panel) line profiles for four slit positions observed for the footpoint region

of jet 1 (Raster 1 - 00:12:33 - 00:16:04 UT). Two or three Gaussian components (blue dashed curves) were used to fit the profiles where the lines were more broad and showed wings.

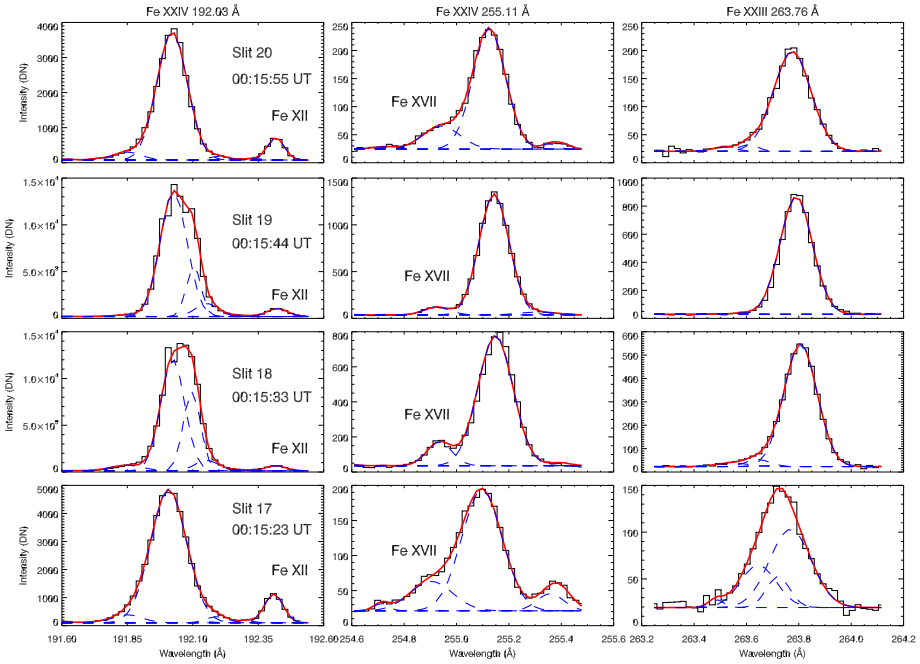

Figure 9. Fe XXIV 192.02 Å (left panel), Fe XXIV 255.11 Å (middle panel) and Fe XXIII 263.76 Å (right panel) line profiles observed during the decay phase of the X-ray C 3.0 class flare at the footpoint region of jet 1 (Raster 1 - 00:12:33 - 00:16:04 UT). The first, second, third and fourth rows show the spectra obtained for the slit positions 20 (00:15:55 UT), 19 (00:15:44 UT), 18 (00:15:33 UT) and 17 (00:15:23 UT) respectively. The curved dashed blue lines represent Gaussian profiles and the fits to the line profiles are shown by red lines.

The Fe XVII 254.87 Å line is close to the Fe XXIV 255.11 Å line. During X-ray flares, both lines get broader and it is difficult to separate and fit the individual line profiles. In this study, the Fe XXIV 255.11 Å line was carefully separated and fitted with a single Gaussian component (see middle panel of fig. 9). The Fe XXIV 192.02 Å line is blended by Fe VIII (Del Zanna, 2009b), Fe XI (Del Zanna, 2010) and an unidentified TR line (Del Zanna, 2009a). The Fe XXIV 192.02 Å line was found to be saturated for two slit positions (see fig 9, slit number 18 and 19) in the raster observed during jet 1 and could not be used for quantitative analysis. So, for further calculations, we used the Fe XXIV 255.11 Å and Fe XXIII 263.76 Å lines. The advantage of using these lines is that both lines are close in wavelength and observed in the long wavelength channel of the EIS instrument. So even if there has been a degradation in the long wavelength channel the lines would have been affected in a similar way.

2.2.3. ***EM Loci Curves for Fe*** XXIII ***and Fe*** XXIV ***Lines***

The *intensity* $I(\lambda_{ji})$ of an optically thin emission line of a wavelength λ_{ji} emitted along the line-of-sight h can be written as

$$I(\lambda_{\rm ji}) = Ab(z) \int N_{\rm e}\ N_H\ C(T, N_{\rm e}, \lambda_{\rm ji})\ dh \tag{1}$$

where $N_{\rm e}$ and N_H are the electron and hydrogen number densities, $C(T, N_{\rm e}, \lambda_{\rm ji})$ is the contribution function of spectral line, $Ab(z)$ is the elemental chemical abundances, and h is the column depth of the emitting plasma along the line-of-sight.

The amount of plasma along the line-of-sight that emits the observed radiation in the temperature between T and $T + dT$ can be expressed as the "column differential emission measure $DEM(T)$"

$$DEM(T) = N_{\rm e}\ N_H\ \frac{dh}{dT} \quad ({\rm cm}^{-5}\ {\rm K}^{-1}) \tag{2}$$

$$\int_T DEM(T)\ dT = \int_h N_{\rm e} N_H\ dh \tag{3}$$

The total column emission measure (EM_{col}) can be calculated by integrating the DEM over the temperature range which was used in the DEM analysis.

$$EM_{\rm col} = \int_h N_{\rm e} N_H\ dh = \int_T DEM(T)\ dT \quad ({\rm cm}^{-5}) \tag{4}$$

The loci of $I_{\rm ob}/G(N_{\rm e}, T, \lambda_{\rm ji})$ curves provide an upper limit to the emission measure distribution as a function of temperature:

$$EM = \frac{I_{\rm ob}}{G(N_{\rm e}, T, \lambda_{\rm ji})} \quad ({\rm cm}^{-5}) \tag{5}$$

Where $G(N_{\rm e}, T, \lambda_{\rm ji}) = Ab(z)\ C(N_{\rm e}, T, \lambda_{\rm ji})$.

If the plasma along the line-of-sight is isothermal, then the EM loci curves for a number of spectral lines should intersect at a single temperature $T_{\rm iso}$ and a single ${\rm EM}_{\rm iso}$ value. The method of analysis assumes that the electron number density ($N_{\rm e}$) and the elemental abundances ($Ab(z)$) do not vary along the line-of-sight. The EM loci curves depend on the instrumental calibration, the accuracy of atomic calculations and the elemental abundances.

Assuming an isothermal plasma ($T = T_{\rm iso}$) along the line-of-sight, we obtained EM loci curves for Fe XXIII 263.76 Å and Fe XXIV 255.11 Å lines. The contribution function of the lines (`gofnt.pro`), calibrated intensities and photospheric abundances (Asplund *et al.*, 2009) and the CHIANTI v.8.0.2 atomic database (Dere *et al.*, 1997; Del Zanna *et al.*, 2015) were used in this calculation. The electron number densities at the footpoint region of jets obtained from the Fe XIV line ratio (see section 2.2.1) were used in this analysis. **The EM Loci method using the contribution functions G(T) for Fe XXIII and Fe XXIV lines does**

not depend on the electron number densities. Therefore, EM values for both lines will remain the same even though we used electron densities from Fe XIV line ratio at a temperature of 1.5-2 MK. In pressure equilibrium, we might expect the N_e values at 10 MK to be about an order of magnitude lower than at 1.5-2 MK. We should also note the multithermal nature of solar flares would suggest that we may be looking at different plasma region. The plasma pressure was calculated at the temperature maximum T_{max} of Fe XXIII and Fe XXIV lines using the equation $P = N_e \times T_{max}$ cm^{-3} K.

Figure 10 shows the EM loci curves for four slit positions which observed the footpoint region of jet 1. The loci curves crossed at very high temperatures between 13.6 and 17.7 MK at different times during the decay phase of the X-ray C 3.0 class flare which was associated with jet 1. The results show that the temperature of the plasma in the footpoint region of jet 1 decreased with time during the decay from 17.7 to 13.6 MK. **We estimate the error in the measured temperature to be around 1 MK.**

A similar analysis was performed for jet 2 for two rasters observed during the impulsive rise and decay phase of the C 1.8 X-ray flare. In the first raster of jet 2, the plasma temperature was found to be increasing from 13.7 to 14.9 MK during the rise phase of the X-ray C 1.8 class flare. For the second raster, the plasma temperature was found to be decreasing during the decay phase of the flare from 14.3 to 13.2 MK. **These changes in temperature within the error limits, so should be treated with caution.**

The plasma temperature and EM values were obtained for four slit positions for both rasters. Table 5 provides details for the Fe XXIII and Fe XXIV lines for both jets. The densities noted in the column 4 are the electron number densities obtained from the Fe XIV line ratio (see section 2.2.1). The Fe XXIII and Fe XXIV line intensities are given in the columns 5 and 6 respectively. The EM values and isothermal temperatures ($T_{\rm iso}$) are given in the columns 7 and 8 respectively.

Assuming a uniform distribution of plasma along the line-of-sight and "spectroscopic filling factor *(f)*"equal to unity, a lower limit to the electron number densities can be estimated using the following equation

$$f = \frac{EM_{col}}{0.83\ N_e^2 h} \tag{6}$$

where N_e is the electron number density in the region and h is the column depth of the emitting plasma along the line-of-sight. Here, we assumed $N_H = 0.83 \times N_e$ considering a fully ionized gas with the relative helium abundance A(He) = 0.1. Considering a cylindrical geometry for the footpoint region of both jets, from the AIA images we estimated a width of 2″ of the structure and obtained these lower limit to electron number densities (see Table 5, column 9). The values obtained **for the 10 MK plasma** are lower than those calculated from the Fe XIV line ratio.

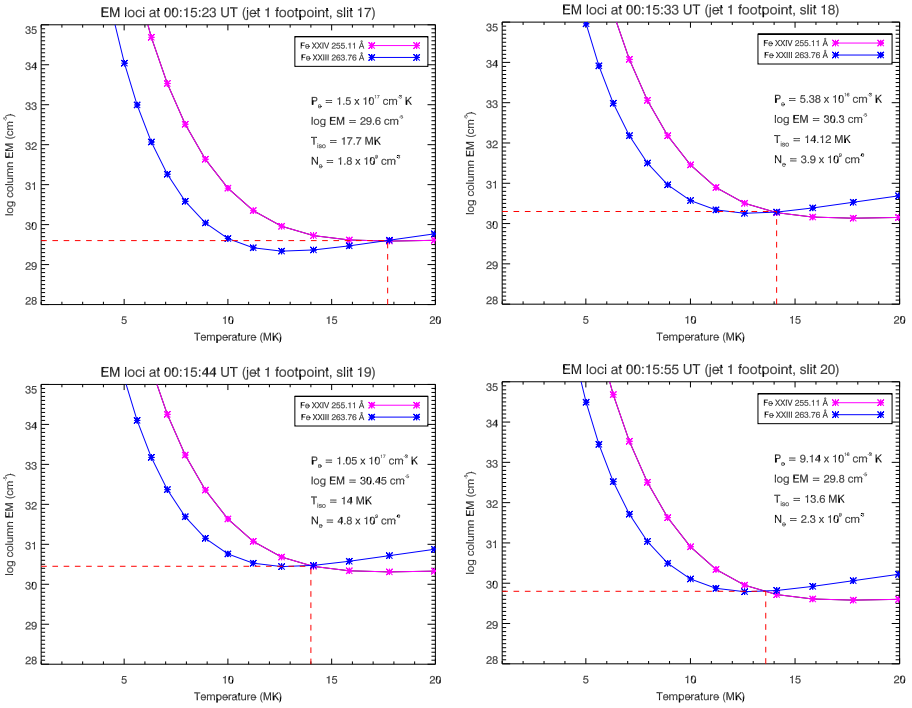

Figure 10. EM loci curves for four slit positions which observed emission from the footpoint region of jet 1. The loci curves for Fe XXIII 263.76 Å and Fe XXIV 255.11 Å lines are shown by blue and pink curves respectively. The dashed red lines represent the isothermal temperatures (crossing) and corresponding values of the emission measure.

*2.2.4. **Nonthermal Velocity Calculation using Fe** XXIII **and Fe** XXIV **Lines***

Figure 9 shows broad spectral profiles for Fe XXIII and Fe XXIV lines during the evolution of both jets. The observed widths were measured from the fitted line profiles. The nonthermal velocities were calculated for the footpoint region of the jets using the isothermal temperature (see Table 5, column 8) obtained from the EM loci plots. The thermal velocity for each line was calculated at the isothermal temperature. The instrumental full-width-half-maximum (FWHM) of 0.058 was used for the long wavelength channel. Table 5 shows nonthermal velocities for Fe XXIV (columns 10) and Fe XXIII (columns 11) lines. The nonthermal velocities ranged from 34 - 100 km/s for Fe XXIV and 51 - 89 km/s for Fe XXIII.

2.3. Temperature Estimate using GOES X-ray Fluxes

The isothermal temperatures obtained from the EM loci plots (see section 2.2.3) during the evolution of both jets were compared with the electron temperatures obtained from the GOES. We used the method developed by Thomas, Crannell,

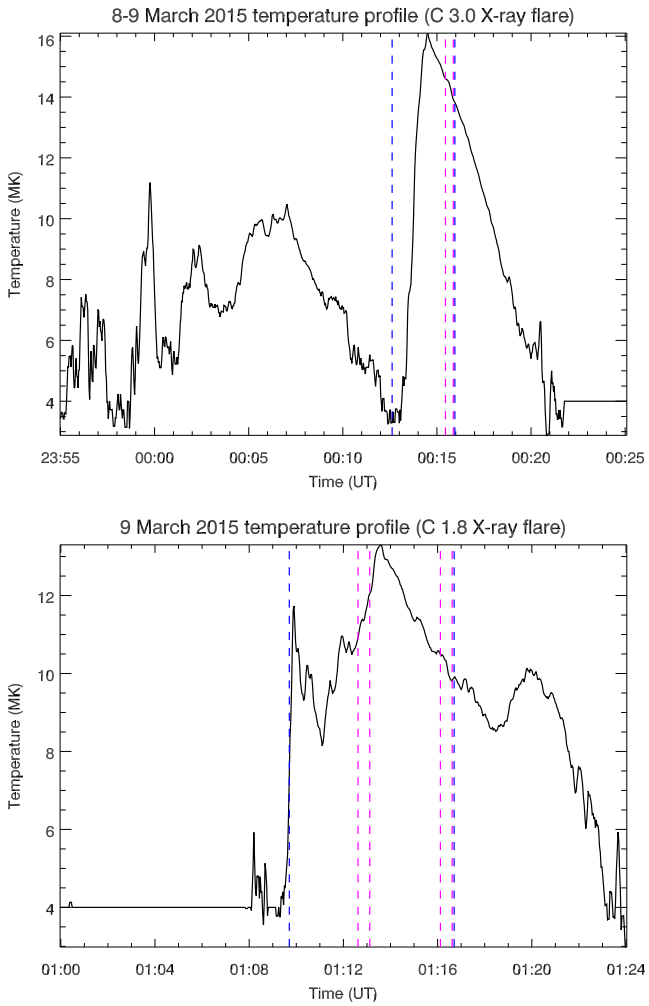

Figure 11. The electron temperature profiles obtained using GOES fluxes observed in two channels during the C 3.0 (during jet 1) (top panel) and C 1.8 (during jet 2) (bottom panel) X-ray flares respectively. The blue and pink dashed lines represent the EIS raster timings, same as shown in the top panel of fig. 4 and fig. 5 respectively.

and Starr (1985) and Garcia (1994) to estimate electron temperatures using the X-ray flux ratio of the GOES 0.5 - 4.0 Å and 1.0 - 8.0 Å channels. The method (Garcia 1994; White, Thomas, and Schwartz 2005) calculates the temperature of an isothermal plasma which would produce the observed ratio of responses in the two GOES channels.

The electron temperature profiles were obtained using the `GOES` package available in the SSW libraries. The X-ray fluxes during the non-flaring/quiet activity on **8 March 2015** from 22:24:00 UT to 22:48:00 UT was selected as a background in the analysis and the electron temperatures were computed.

Figure 11 shows the electron temperature profiles obtained for both flare events. The blue and pink dashed lines represent the EIS raster timings (as shown in the top panels of figs. 4 and 5). The electron temperature from GOES data was found to be decreasing from 15 to 14 MK during the decay phase of the C 3.0 flare which was observed during jet 1 (the timings are shown by the pink dashed lines in the top panel). We found that the temperature was rising from 11 to 12 MK during the impulsive phase and decreasing from 10.5 to 9.8 MK during the decay phase of the C 1.8 flare (the timings are shown by the pink dashed lines in the bottom panel) which was observed during jet 2.

However, we estimate an error of around 0.4 MK for these measurements (Garcia, 1994). This means that the increase and decrease measures should be treated with caution. The isothermal temperatures at the footpoint region of both jets obtained from the EM loci using Fe XXIII and Fe XXIV were found to be in good agreement (within 20% uncertainty) with the electron temperatures obtained by the GOES flux ratio.

Feldman *et al.* (1996) studied flares seen by GOES in the 1 - 8 Å channel and found that there is a linear relationship between X-ray class flares and the electron temperature obtained at the peak of the flares using the Bragg Crystal Spectrometer (BCS) on board Yohkoh (Ogawara *et al.*, 1991). We recorded peak temperatures ranging from 12.5 to 18.5 MK for both C 3.0 and C 1.8 flares. The isothermal temperatures (see section 2.2.3) and electron temperatures obtained here show good agreement with and are within the range of temperatures reported by Feldman *et al.* (1996).

2.4. X-ray Imaging Results using RHESSI

On 8 and **9 March 2015**, the RHESSI instrument was in the night time during 23:50 - 00:25 UT and so it could not observe X-ray emission during the evolution of jet 1. The RHESSI observed soft and hard X-ray emission during the evolution of jet 2.

Figure 12 shows spin-averaged corrected count rates with 4 sec resolution obtained in the 3-6 (pink curve), 6-12 (blue curve) and 12-25 keV (green curve) energy channels by taking an average over all nine detectors. The GOES X-ray flux in the 0.5 - 4.0 Å (black curve) and 1.0 - 8.0 Å (red curve) channels are also overplotted for comparison. The RHESSI soft (3-6, 6-12 keV) and hard (12-25 keV) X-ray curves follow the same activity as the X-ray C 1.8 class flare observed by the GOES instrument. The results confirm that there is a temporal correlation between the flare activity and hard X-ray emission.

Table 5. Plasma parameters obtained from Hinode EIS

col. 1	col. 2	col. 3	col. 4	col. 5	col. 6	col. 7	col. 8	col. 9	col. 10	col. 11
Event	Time (UT)	Y (pixel)	Density (N_e cm^{-3})	I(Fe XXIV) (255.11 Å)	I(Fe XXIII) (263.76 Å)	log EM (cm^{-5})	T_{iso} (MK)	estimated (N_e cm^{-3})	Non-thermal width (km/s) (Fe XXIV)	(Fe XXIII)
AR Jet 1 - Raster 1 - Start time - 00:12:33 UT and End time - 00:16:04 UT										
slit 17	00:15:23	119:127	4.7×10^{10}	5417	732	29.60	17.7	1.8×10^{9}	100	81
slit 18	00:15:33	123:133	2.7×10^{10}	19015	6073	30.30	14.12	3.9×10^{9}	85	70
slit 19	00:15:44	129:143	5.3×10^{10}	28536	9352	30.45	14.0	4.8×10^{9}	58	63
slit 20	00:15:55	140:148	4.6×10^{10}	5328	2077	29.80	13.6	2.3×10^{9}	71	88
AR Jet 2 - Raster 1 - Start time - 01:09:41 UT and End time - 01:13:12 UT										
slit 17	01:12:31	121:130	2.6×10^{10}	580	216	28.8	13.7	7.2×10^{8}	34	69
slit 18	01:12:42	123:133	1.7×10^{10}	1856	691	29.3	13.7	1.3×10^{9}	36	67
slit 19	01:12:52	127:140	2.0×10^{11}	1834	689	29.3	13.7	1.3×10^{9}	80	89
slit 20	01:13:03	129:141	3.2×10^{10}	1613	399	29.15	14.9	1.1×10^{9}	93	76
AR Jet 2 - Start time - 01:13:15 UT and End time - 01:16:46 UT										
slit 17	01:16:05	120:130	2.0×10^{10}	732	213	28.85	14.3	7.7×10^{8}	49	58
slit 18	01:16:15	125:135	2.1×10^{10}	886	455	29.15	12.85	1.1×10^{9}	34	51
slit 19	01:16:26	127:140	4.4×10^{10}	1561	664	29.3	13.3	1.3×10^{9}	54	58
slit 20	01:16:37	133:148	4.1×10^{10}	1608	723	29.35	13.2	1.4×10^{9}	55	80

Notes. $T_{\rm iso}$ - isothermal temperature where EM loci curves for Fe XXIII and Fe XXIV lines intersect, Columns 5 and 6 - intensities of EIS lines in erg cm^{-2} s^{-1} sr^{-1} Å^{-1} units, Column 4 - $N_{\rm e}$ from Fe xiv, Colum 9 - lower limit on $N_{\rm e}$ from EM.

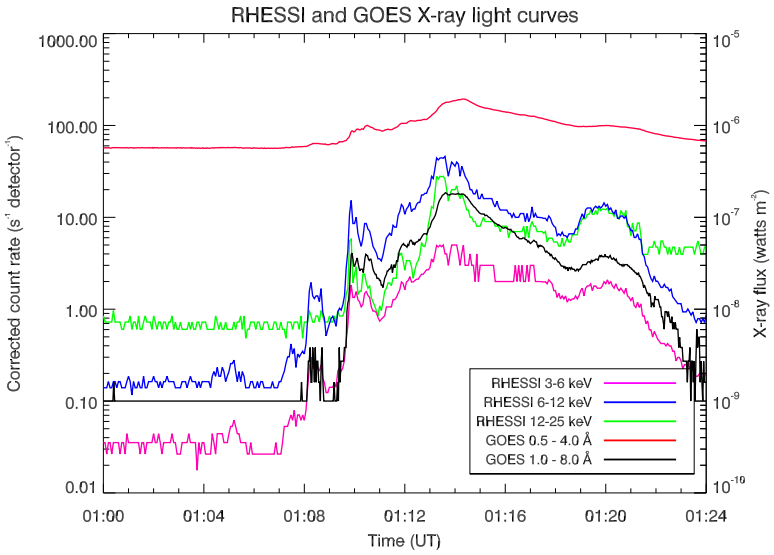

Figure 12. RHESSI light curves in the 3-6 (pink), 6-12 (blue) and 12-25 keV (green) channels observed during the evolution of jet 2. The left Y-axis represents RHESSI corrected count rates. The GOES X-ray fluxes in the 0.5 - 4.0 Å (red) and 1.0 - 8.0 Å (black) channels for C 1.8 flare are also plotted in this plot for comparison. The right Y-axis represents GOES X-ray fluxes for C 1.8 flare.

In order to find the spatial correlation between the hard X-ray emission observed by RHESSI and the evolution of the footpoint region of jet 2, we have created X-ray images using RHESSI detectors 4-8. We used an image reconstruction method based on the CLEAN algorithm (Hurford *et al.*, 2002).

Figure 13 shows AIA 171 Å images during the evolution of the AR jet 2. The images of the RHESSI X-ray sources were created by taking an average over the fluxes observed during 01:07:00 - 01:09:04 UT (row 1), 01:09:00 - 01:11:04 UT (row 2) and 01:11:00 - 01:14:04 UT (row 3). The sources were observed at the footpoint region of jet 2 and they are plotted as contours on the AIA 171 Å images. The cyan (left panel) and yellow colour (middle panel) contours represent soft X-ray emission in the 3-6 and 6-10 keV energy channels respectively. The green contours (right panel) represent hard X-ray emission in the 12-25 keV energy channel. From RHESSI light curves as well as from the imaging, it is clear that the hard X-ray emission at the footpoint of a jet 2 started a bit later (∼2 min) at 01:10:11 UT. The soft and hard X-ray sources were confined to the footpoint region of jet 2.

2.4.1. ***Spectroscopic Results from FERMI***

By taking advantage of the Gamma-ray Burst Monitor (GBM) on the Fermi Gamma-ray Space Telescope[5] (Atwood *et al.*, 2009), we performed further analysis

[5]https://hesperia.gsfc.nasa.gov/fermi_solar/

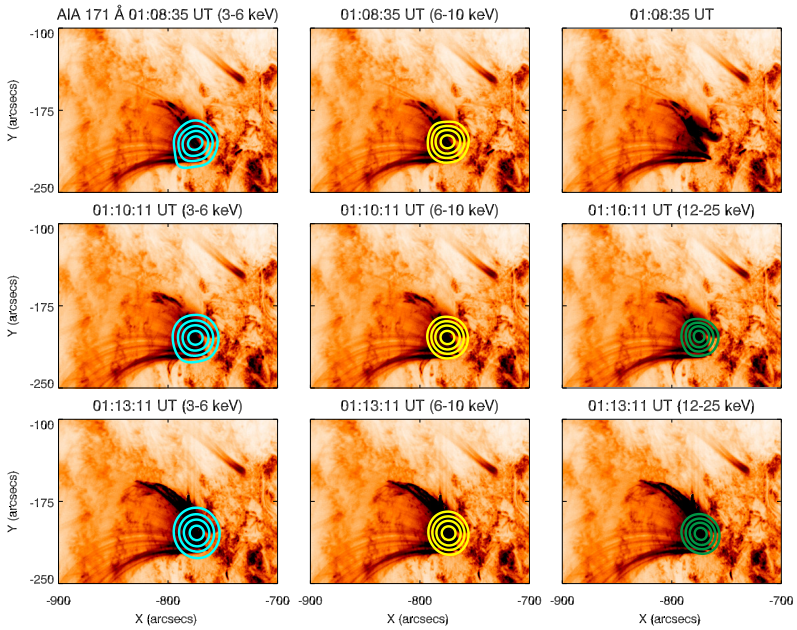

Figure 13. AIA 171 Å images during the evolution of the AR jet 2. The timings mentioned in the images are the AIA 171 Å image timings. The X-ray sources were observed at the footpoint region of jet 2. The cyan (left panel) and yellow colour (middle panel) contours represent soft X-ray emission observed by the RHESSI in the 3-6 and 6-10 keV energy channels respectively. The green contours (right panel) represent hard X-ray emission in the 12-25 keV energy channel. The images of the RHESSI X-ray sources were created by taking an average over the fluxes observed during 01:07:00 - 01:09:04 UT (row 1), 01:09:00 - 01:11:04 UT (row 2) and 01:11:00 - 01:14:04 UT (row 3). All contours are plotted as 30, 50, 70 and 90% of peak flux in each energy channel.

of soft and hard X-ray emission and also studied the temperature distribution during both jet events using FERMI spectra.

The most sunward directed detectors NaI05 and NaI00 were used to capture emission during jet 1 and jet 2 respectively. Figure 14 shows emission observed by the FERMI GBM in its various energy bands during both flares[6] (start time : 00:13:32 UT (01:12:37), peak time : 00:14:28 UT (01:13:18), end time : 00:15:25 UT (01:15:12)). The SSW package OSPEX[7] was used to generate light curves and also to fit the spectra. Fermi captured emission during the impulsive rise and peak phase C 3.0 flare (i.e. during jet 1) and entire C 1.8 flare (i.e. during jet 2).

The hard X-ray emission was also observed by FERMI during jet 1 activity (see fig. 14, top panel). Since all AIA channels showed very similar signatures for both jet events, we assumed that this hard X-ray emission also originated at

[6]https://hesperia.gsfc.nasa.gov/fermi/gbm/qlook/fermi_gbm_flare_list.txt

[7]http://sprg.ssl.berkeley.edu/~tohban/wiki/index.php/OSPEX_Users_Guide

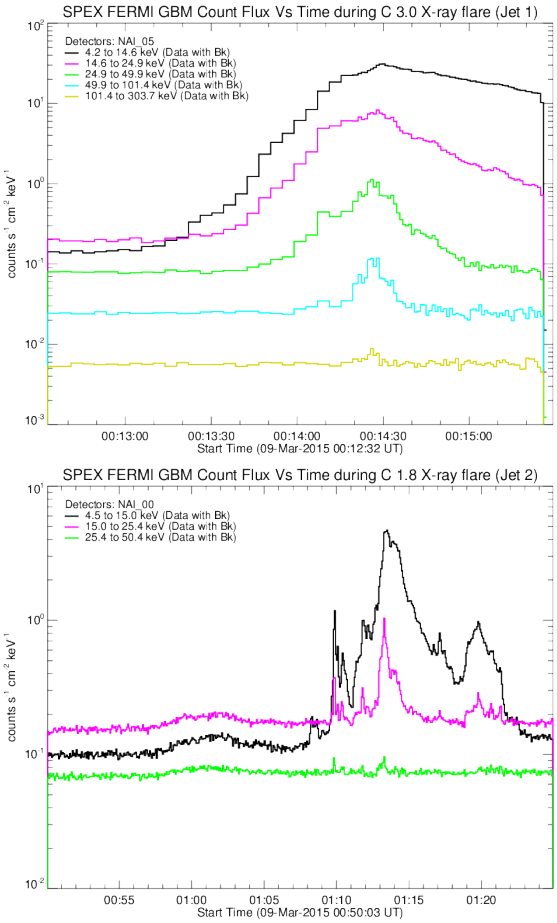

Figure 14. FERMI GBM light curves during jet 1 (top panel) and jet 2 (bottom panel) events.

the footpoint region of jet 1, similar to the hard X-ray sources seen during jet 2 (see fig. 13). We assumed that the photon spectrum measured by FERMI can be taken to represent emission from a compact X-ray source in the case of both jets, and for consistency we performed a spectroscopic analysis for both jets using the FERMI data. For both events background subtraction was performed and the spectra were fitted with a combination of a thermal plus thick target function.

For jet 1, the spectra in two time intervals could be fitted: 00:13:17 - 00:13:58 UT and 00:13:58 - 00:14:37 UT. The measured spectra with fits overlaid are shown in Figure 15. Note that the Iodine K-edge at 33.17 keV can, at high count rates, be seen as a discontinuity in the FERMI GBM spectra, and can produce large residuals around this energy when the spectra are fitted. However, while this contributes to producing a larger than desirable χ^2 value for the fits, it does not cause a bias in the fit parameters (Bissaldi *et al.*, 2009). This effect was apparent in some of the spectra observed during jet 2. For jet 1, the nonthermal

energy calculated using the derived fit parameters was 2.38×10^{26} erg s^{-1} for the first time interval (00:13:17 - 00:13:58 UT) and 2.87×10^{27} erg s^{-1} for the second time interval (00:13:58 - 00:14:37 UT). The plasma temperature derived from the fitting for jet 1 is 27 MK for the first time interval and 25 MK second time interval. These measurements were made slightly before the EIS raster scan started at 00:15:23 UT, but are consistent with the decreasing temperature measure with EIS.

For jet 2, it was possible to fit the spectrum at 40 sec accumulation times from 01:09:14 to 01:23 UT. Again the spectra were fitted with a combination of a thermal and thick target function, and from the spectral fits, we derived the nonthermal energy deposition with time, as shown in Figure 16 (left panel). From this and Figure 14, it can be seen that the emission is predominantly thermal between 01:09 and 01:14 UT, while a nonthermal component dominates coincident with the main X-ray peaks. Figure 16 (right panel) shows the plasma temperature derived from the spectral fitting for jet 2, and it can be seen that the highest jet temperatures are seen earliest in the event, gradually decreasing as the nonthermal component of the X-ray emission increases. The peak jet temperature at 01:09 UT is 29 MK, of similar order to those found by Bain and Fletcher (2009); Christe, Krucker, and Lin (2008) in their studies, and indicating an association of the jet with the presence of superhot plasma. The temperature can then be seen to drop, but there is a second lower peak around 01:13 UT, as can also be seen in Table 4 for the temperatures derived from EIS observations.

2.5. The Evolution of the Photospheric Magnetic Field during Jets

Jets are thought to be driven by magnetic reconnection between a closed magnetic loop and open background magnetic fields. Due to this reconnection, new closed loops are generated. Flux cancellation associated with jets is usually caused by submergence of this new closed loop (Chifor *et al.*, 2008).

Figure 17 shows reverse colour images in the AIA 1600 Å channel at the time of jet 1 and jet 2, respectively. Red and blue contours stand for positive and negative line-of-sight (LOS) magnetic field (±200 G) obtained with the Helioseismic Magnetic Imager (HMI; Schou *et al.* 2012, Scherrer *et al.* 2012). The HMI obtained LOS magnetic field data with high-resolution (0.5″ per pixel) and high-cadence (45 seconds) from **8^{th} March 22:30 UT to 9^{th} 02:30 UT**. The Solarsoft routine `aia_prep.pro` was applied for data obtained by the AIA and HMI for the purpose of calibration and co-alignmnet. These images show ribbon-like structure and reflect that recurrent jets rose from the highly mixed-polarity region. Figure 18 shows reverse color images in the AIA 94 Å channel at the time of jet 1 and jet 2 which indicate post-flare closed loops. The green lines show intensity contours of the AIA 1600 Å images, representing flare ribbons. It can be seen that flare ribbons appear at footpoints of post-flare loop seen in the AIA 94 Å image.

Figure 19 shows the HMI LOS magnetograms at the time of jet 1 and jet 2. Note that, since the active region was located away from disk center at the time, the accuracy of LOS magnetogram is not very good. In fig. 19, we label the positive polarity regions associated with flare ribbons with P1 and P2 and the negative

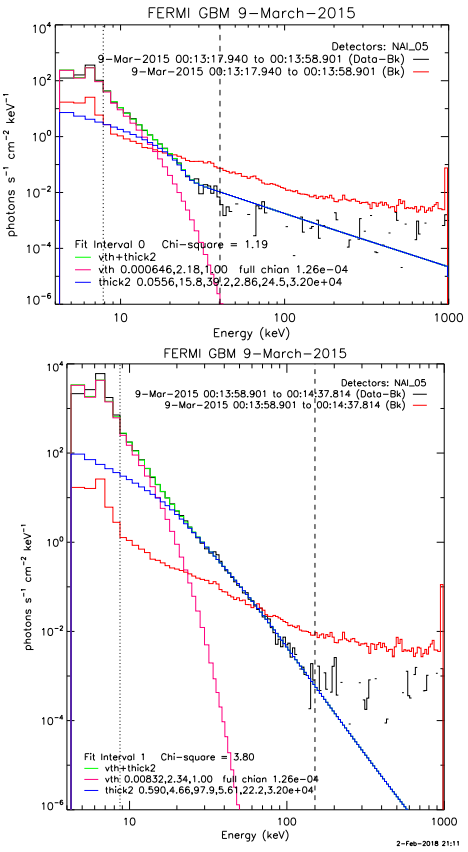

Figure 15. The combined thermal and thick target spectral fit to FERMI GBM data for the intervals 00:13:17 - 00:13:58 UT (top panel) and 00:13:58 - 00:14:37 UT (bottom panel) during jet 1.

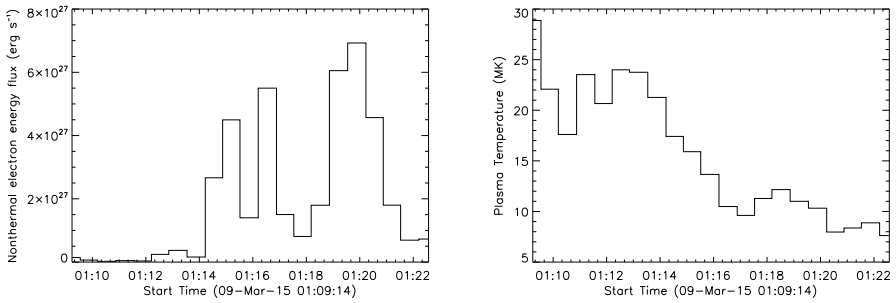

Figure 16. Non-thermal energy flux calculated from a thick target model (left panel) and plasma temperature derived from the FERMI spectral fits for jet 2.

polarity region associated with flare ribbons with N1. **These boxes move in accordance with the Sun's rotation.** Comparing the LOS magnetograms, fig. 17, and 18, we speculate that the loop connecting the positive region in P1 and the negative region in N1 is a pre-existing closed loop and positive open fields from a main sunspot and the positive fields in P2 collimate the ejecta of jets.

Figure 20 shows the temporal evolution of the magnetic field in the period studied. Although the boxes are set in the complex region, magnetic elements in the boxes do not move significantly. For example, negative polarity elements are located within the N1 box. Thus, any major changes in the temporal evolution of the magnetic flux are not caused by the proper motions of magnetic elements through the boundary of the boxes.

We calculate the temporal evolution of LOS positive magnetic flux in P1 and P2 and negative magnetic flux in N1 **in about 4 hours covering the time of the jets** to investigate the relationship between the occurrence of jets and magnetic field. Figure 21 shows the time profile of LOS magnetic flux in N1, P1 and P2. When these magnetic flux were calculated, negative flux in P1 and P2, and positive flux in N1, were neglected. **Additionally, to eliminate effects of noises, we also neglect weak flux whose flux is less than the noise level of the HMI 45-second magnetogram, namely, 10 G (Liu *et al.*, 2012). Two green lines represent the time when jet 1 and jet 2 occurred.**

Regarding the long-term evolution, Magnetic flux in P2 shows an increasing tendency before jet 1 and jet 2. After jet 2, however, the flux shows a significant decrease. This decreasing tendency can be seen in the behavior of magnetic flux in N1, nonetheless this is gentle. On the other hand, in P1, magnetic flux does not decrease drastically soon after the jets.

Regarding the short-term evolution, absolute magnetic flux in N1 shows a sharp decrease during jet 1 and jet 2. The timescale of the decrease is about 5-10 minutes. In P2, similarly, absolute magnetic flux decreases during jet 1 and after jet 2. In P1, on the other hand, the absolute flux decreases about 20 or 15 minutes before jet 1 and 2, respectively. Moreover, after the decreases, the flux significantly increases during jet 1, and before jet 2. These sharp increases could be the onset of the jets. Note that short-term increases and decreases can be found at different times from these of jet 1 and 2. This could be related to other jets which occur frequently in the region but are not included in this study.

In P2, the magnitude of the increase or decrease is about 0.2×10^{19} Mx. This value is small, however, considering the noise level of 10 G, we can estimate the magnitude of fluctuation due to noise at about 0.3×10^{18} Mx. Therefore, we consider that the increase and decrease are associated with the jet activity, not the noise.

Figure 22 shows a schematic model representing our speculation on the jets, based on the model by Chifor *et al.* (2008). From the EUV images, it can be assumed that P1 and N1 are connected with closed fields. The fields interact with the open fields of P2 and magnetic reconnection occurs. The reconnection flow

heats the chromosphere and the jets are ejected, being collimated by the open fields of P2 and the vertical fields of the sunspot. The new closed field connecting P2 and N1 may submerge and cancel. We believe that the decreasing behavior of the magnetic flux in P2 and N1 reflects this cancellation.

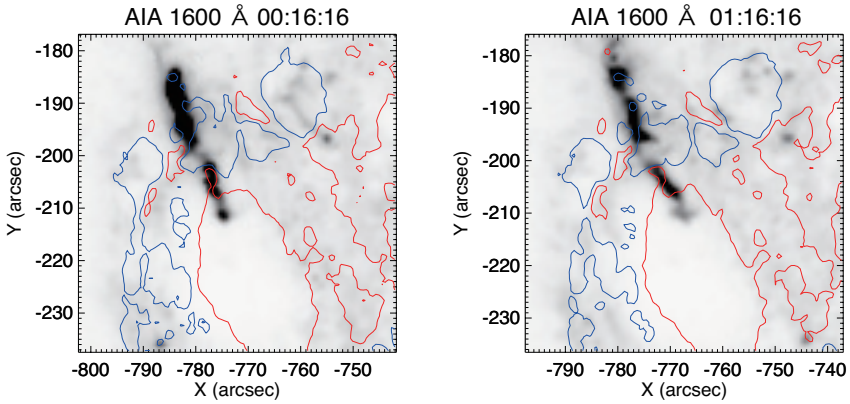

Figure 17. AIA 1600 Å images at the time of jet 1 (left panel) and jet 2 (right panel), indicating flare ribbons. Red (blue) lines are contours of LOS positive (negative) magnetic field of ±200 G.

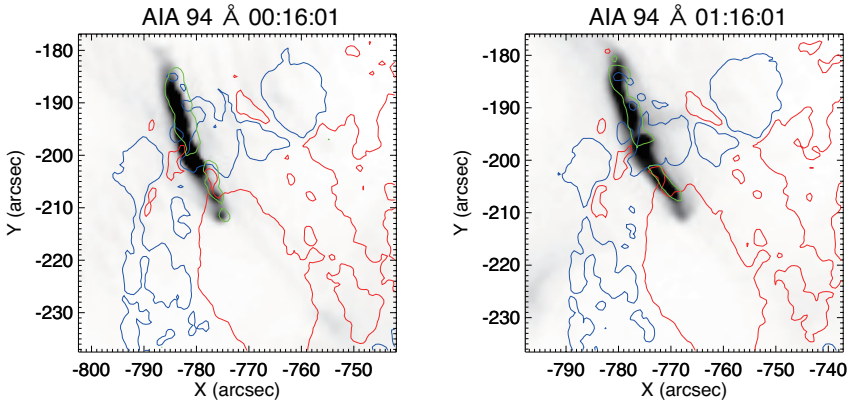

Figure 18. AIA 94 Å images at the time of jet 1 (left panel) and jet 2 (right panel), indicating closed post-flare loops. Green contours are indicating flare ribbons from AIA 1600 Å. Red (blue) contours represent LOS positive (negative) magnetic field of ±200 G.

3. Discussion and Summary

Simultaneous observations from the EIS, AIA, FERMI and RHESSI instruments presented in this paper provided clear evidence for the existence of flare like temperatures (>10 MK) and soft/hard X-ray emission at the footpoint region of a recurrent AR jet. The GOES instrument observed two C-class flares (see

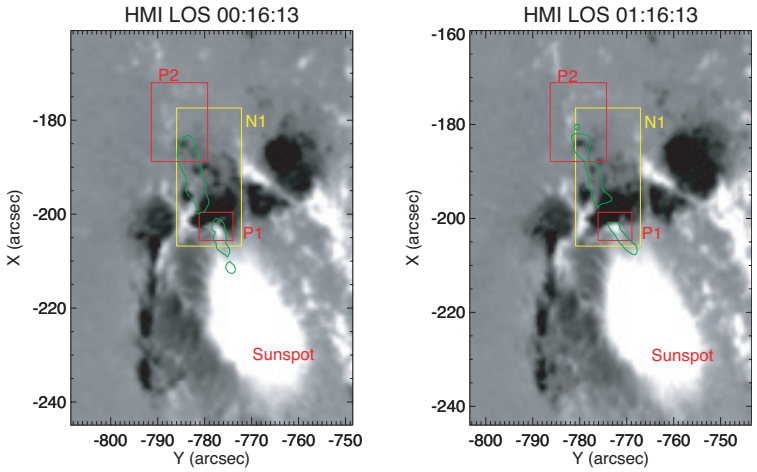

Figure 19. HMI LOS magnetic field at the time of jet 1 (left panel) and jet 2 (right panel), showing the magentic field of ±500 G. P1 **(small red box)** and P2 **(big red box)** are determined to calculate flare-related positive magnetic flux. N1 **(yellow box)** is determined to calculate flare-related negative magnetic flux. **The green contours are indicating flare ribbons from AIA 1600 Å.**

top panels of figs. 4 and 5) during the recurrent jet activity. The temporal and spatial correlation between flares and footpoint activity of the recurrent AR jet has been confirmed using EIS observations (emission in Fe XXIII and Fe XXIV lines) and AIA light curves (see bottom panels of figs. 4 and 5). As far as we are aware, this is the first clear case of hot flare emission in an active region jet observed with EIS.

Multithermal plasma was observed in all AIA channels (see figs. 2 and 3) as well as in EIS observations. The AIA 94 Å channel was found to be dominated by Fe XVIII emission whereas the AIA 131 Å was most likely to be dominated by Fe XXI emission. The plane-of-sky velocities for ∼0.7 MK plasma were found to be **462±21** and **228±23 km/s** for jet 1 and 2 (see fig. 6) respectively. The RHESSI light curves obtained for jet 2 show a good temporal correlation with the X-ray flare. The RHESSI images confirmed that the soft and hard X-ray sources were located at the footpoint region of jet 2.

The EM loci curves for Fe XXIII and Fe XXIV lines showed that the plasma at the footpoint region was cooling from 17.7 to 13.6 MK (for jet 1) during the decay phase of the C3.0 flare. **We estimate the error in the measured temperature to be around 1 MK.** The plasma temperature was increasing (then decreasing) from 13.7 to 14.9 MK (then from 14.3 to 13.2 MK) (for jet 2) during the rise (decay) phase of the C1.8 flare. **These changes in temperature within the error limits, so should be treated with caution.** These temperatures show very good agreement with electron temperatures obtained using GOES flux ratio of 0.5 - 4.0 Å and 1.0 - 8.0 Å channels and they are within the range of temperatures reported by Feldman *et al.* (1996) for flares in general.

The Fe XXIII and Fe XXIV (both lines) line profiles were broader than their thermal widths and the nonthermal velocities ranged from 34-100 km/s for

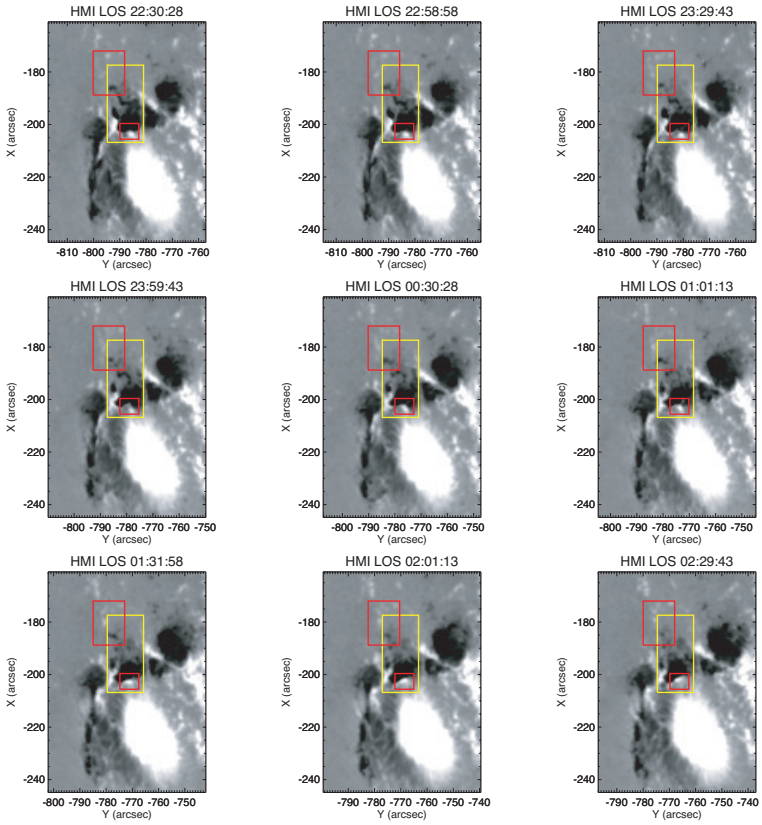

Figure 20. The evolution of magnetic field of ±500 G from 8^{th} March 22:30 UT to 9^{th} 02:30 UT. Red and yellow boxes are the same as those in figure 19.

Fe XXIV and 51-89 km/s for Fe XXIII. The nonthermal velocities obtained from the Fe XXIV show good agreement with those obtained by Doschek *et al.* (2015) in their individual study of M-class flare which showed surge like plasma ejection. The electron number density values obtained in the footpoint region of jet 1 and 2 were found to be lower than the values obtained for the jet studied in Mulay, Del Zanna, and Mason (2017b) and Doschek *et al.* (2015), but show good agreement with the values obtained for the jet studied in Mulay *et al.* (2016). The superhot plasma of 27 (25) MK was confirmed by FERMI during the rise (peak) phase of jet 1 whereas; peak temperature of 29 MK was measured at jet 2. These results showed a good agreement with those obtained by Bain and Fletcher (2009), Christe, Krucker, and Lin (2008) and Doschek *et al.* (2015).

The comparison of AIA 1600 Å images and the HMI LOS magnetograms showed that ribbon-like brightening structures appeared in the highly mixed-polarity region at the times of jet 1 and 2. Regarding magnetic field, **the LOS magnetic flux in P1 showed a sudden increase at both of the jets. We consider this could be the onset of these jets.** The LOS magnetic flux in P2 (see fig. 19) drastically decreased after jet 2 **in the short timescale. A**

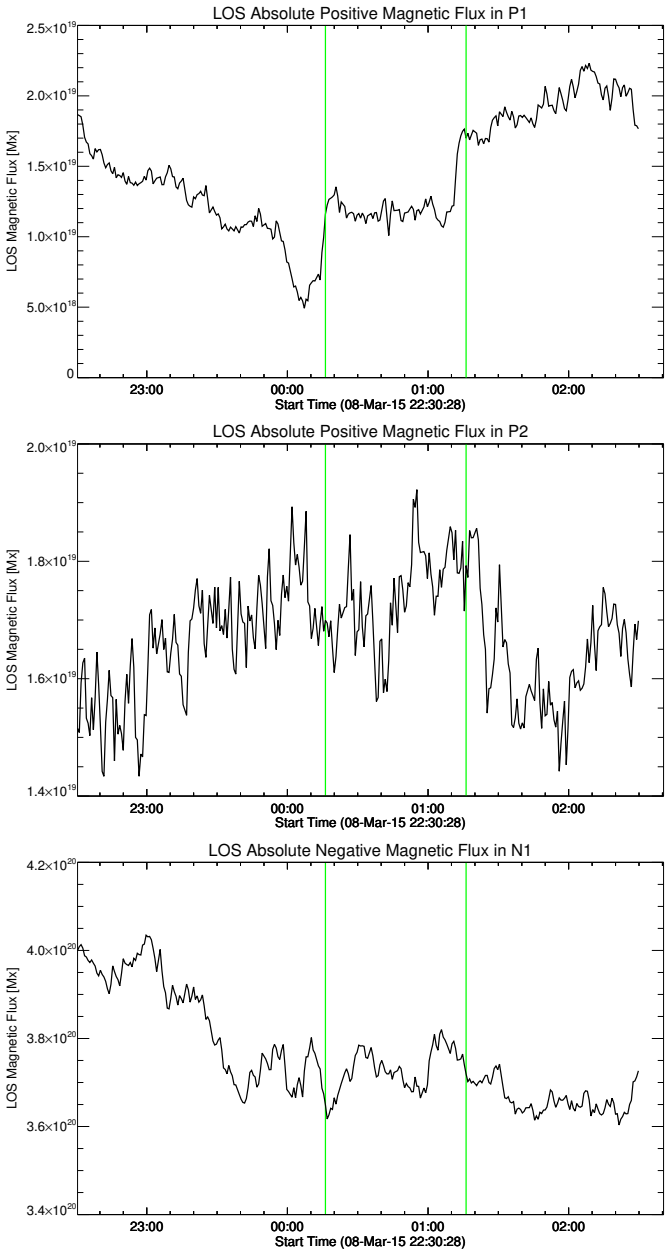

Figure 21. The unsigned LOS magnetic field evolution in (top panel) P1, (middle panel) P2, and (bottom panel) N1 from 8^{th} March 22:30 UT to 9^{th} 02:30 UT. Two green lines represent the time when jet 1 and jet 2 occurred.

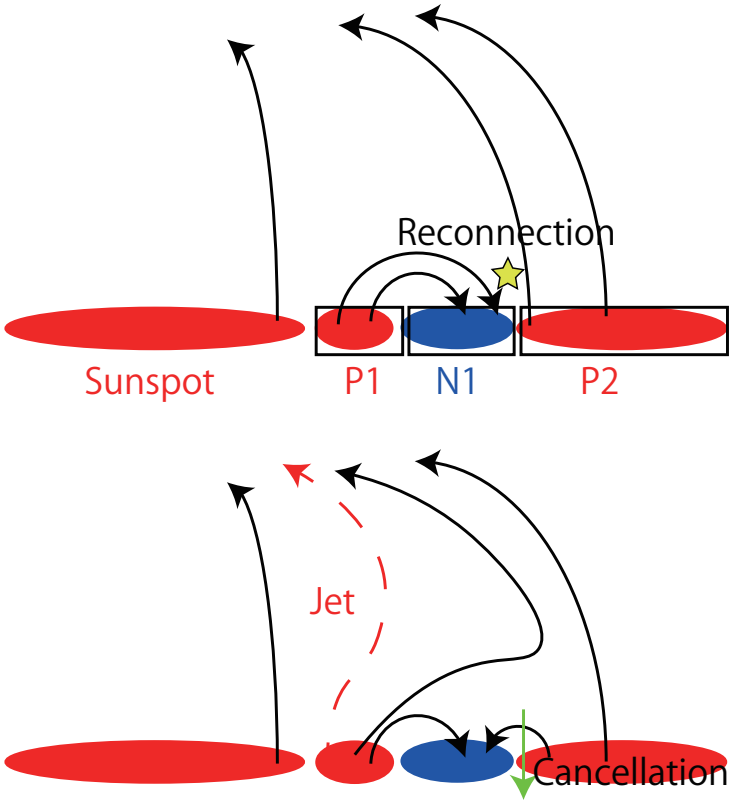

Figure 22. Schematic model of jets based on Chifor *et al.* (2008). We speculate magnetic reconnection between open fields of P2 and closed loops connecting P1 and N1 drive the jets. The jet seen in the EUV band is ejected along the red dashed line. New closed loops connecting P2 and N1 submerge and cancel, as seen in fig. 21 in the form of the decrease of the absolute magnetic flux.

long-term decreasing tendency can also be seen. In N1, **a short-time sharp decrease occur both during jet 1 and 2, and long-term** gentle decrease of LOS magnetic flux occurred during jet 2. We consider this decreasing tendency reflects jet-related flux cancellation. Based on the results and EUV/UV images obtained by AIA, we suggested a picture (see fig. 22) explaining the jets in the same way as Chifor *et al.* (2008). We consider that plasma was heated by reconnection downflow, ejected, and collimated by the background and sunspot's positive open fields.

In this study, EIS observations provided a unique opportunity to study very hot plasma (up to ∼18 MK observed during decay phase of flare) at the footpoint of two jets but it is still unclear as to whether the hot emission is only confined to the footpoint region or the hot plasma also travels along the spire structure. Other questions remain. Do AR jets get hotter than 29 MK? Why are such high temperatures present only in a few jets? Does the magnetic complexity of the active region have any role in producing X-ray flares in the footpoint region of a

jet? Do higher class X-ray flares (above C-class) associated with AR jets show similar and/or higher temperatures? In order to investigate these questions, we need a number of spectroscopic observations which cover emission from the spire as well as footpoint region of AR jets. Further co-ordinated AR jet observations with Hinode, RHESSI/FERMI spectroscopic observations and observations from the upcoming solar mission Solar Orbiter (Müller *et al.*, 2013) (on board the ***Spectrometer Telescope for Imaging X-rays*** (STIX) (Benz *et al.*, 2012)) may provide important insights into our understanding of the high temperature component of AR jets.

Acknowledgments The data analysis and results presented in this paper are an outcome of collaborative work. The work was carried out when one of the authors, S.M.M. was a Ph.D. student at the University of Cambridge, UK. This work (except FERMI and HMI data analysis) has been included in her Ph.D. thesis as Chapter 9. This project was funded by the Daiwa Anglo-Japanese Foundation (DAIWA)-Adrian award. SMM acknowledges support from the Cambridge Trust, University of Cambridge, UK. HEM, GDZ and SAM (grant number ST/N000722/1) acknowledge the support of STFC. AIA data are courtesy of SDO (NASA) and the AIA consortium. CHIANTI is a collaborative project involving George Mason University, the University of Michigan (USA) and the University of Cambridge (UK). Hinode is a Japanese mission developed and launched by ISAS/JAXA, with NAOJ as domestic partner and NASA and STFC (UK) as international partners. It is operated by these agencies in co-operation with ESA and NSC (Norway). We acknowledge the RHESSI team for the open access to the data. We also acknowledge the use of Fermi Solar Flare Observations facility which is funded by the Fermi GI program (http://hesperia.gsfc.nasa.gov/fermi_solar/).

Disclosure of Potential Conflicts of Interest - The authors declare that they have no conflicts of interest.

References

Asplund, M., Grevesse, N., Sauval, A.J., Scott, P.: 2009, The Chemical Composition of the Sun. **47**, 481. DOI. ADS.

Atwood, W.B., Abdo, A.A., Ackermann, M., Althouse, W., Anderson, B., Axelsson, M., Baldini, L., Ballet, J., Band, D.L., Barbiellini, G., et al.: 2009, The Large Area Telescope on the Fermi Gamma-Ray Space Telescope Mission. *Astrophys. J.* **697**, 1071. DOI. ADS.

Bain, H.M., Fletcher, L.: 2009, Hard X-ray emission from a flare-related jet. *Astron. Astrophys.* **508**, 1443. DOI. ADS.

Benz, A.O., Krucker, S., Hurford, G.J., Arnold, N.G., Orleanski, P., Gröbelbauer, H.-P., Klober, S., Iseli, L., Wiehl, H.J., Csillaghy, A., Etesi, L., Hochmuth, N., Battaglia, M., Bednarzik, M., Resanovic, R., Grimm, O., Viertel, G., Commichau, V., Meuris, A., Limousin, O., Brun, S., Vilmer, N., Skup, K.R., Graczyk, R., Stolarski, M., Michalska, M., Nowosielski, W., Cichocki, A., Mosdorf, M., Seweryn, K., Przepiórka, A., Sylwester, J., Kowalinski, M., Mrozek, T., Podgorski, P., Mann, G., Aurass, H., Popow, E., Onel, H., Dionies, F., Bauer, S., Rendtel, J., Warmuth, A., Woche, M., Plüschke, D., Bittner, W., Paschke, J., Wolker, D., Van Beek, H.F., Farnik, F., Kasparova, J., Veronig, A.M., Kienreich, I.W., Gallagher, P.T., Bloomfield, D.S., Piana, M., Massone, A.M., Dennis, B.R., Schwarz, R.A., Lin, R.P.: 2012, The spectrometer telescope for imaging x-rays on board the Solar Orbiter mission. In: *Space Telescopes and Instrumentation 2012: Ultraviolet to Gamma Ray*, **8443**, 84433L. DOI. ADS.

Bissaldi, E., von Kienlin, A., Lichti, G., Steinle, H., Bhat, P.N., Briggs, M.S., Fishman, G.J., Hoover, A.S., Kippen, R.M., Krumrey, M., Gerlach, M., Connaughton, V., Diehl, R., Greiner, J., van der Horst, A.J., Kouveliotou, C., McBreen, S., Meegan, C.A., Paciesas, W.S., Preece, R.D., Wilson-Hodge, C.A.: 2009, Ground-based calibration and characterization of the Fermi gamma-ray burst monitor detectors. *Experimental Astronomy* **24**, 47. DOI. ADS.

Brosius, J.W.: 2013, Rapid Evolution of the Solar Atmosphere during the Impulsive Phase of a Microflare Observed with the Extreme-ultraviolet Imaging Spectrometer aboard Hinode: Hints of Chromospheric Magnetic Reconnection. *Astrophys. J.* **777**, 135. DOI. ADS.

Chae, J., Qiu, J., Wang, H., Goode, P.R.: 1999, Extreme-Ultraviolet Jets and Hα Surges in Solar Microflares. *Astrophys. J. Lett.* **513**, L75. DOI. ADS.

Chandra, R., Gupta, G.R., Mulay, S., Tripathi, D.: 2015, Sunspot waves and triggering of homologous active region jets. *Mon. Not. Roy. Astron. Soc.* **446**, 3741. DOI. ADS.

Chen, N., Ip, W.-H., Innes, D.: 2013, Flare-Associated Type III Radio Bursts and Dynamics of the EUV Jet from SDO/AIA and RHESSI Observations. *Astrophys. J.* **769**, 96. DOI. ADS.

Chifor, C., Young, P.R., Isobe, H., Mason, H.E., Tripathi, D., Hara, H., Yokoyama, T.: 2008, An active region jet observed with Hinode. *Astron. Astrophys.* **481**, L57. DOI. ADS.

Christe, S., Krucker, S., Lin, R.P.: 2008, Hard X-Rays Associated with Type III Radio Bursts. *Astrophys. J. Lett.* **680**, L149. DOI. ADS.

Culhane, J.L., Harra, L.K., James, A.M., Al-Janabi, K., Bradley, L.J., Chaudry, R.A., Rees, K., Tandy, J.A., Thomas, P., Whillock, M.C.R., Winter, B., Doschek, G.A., Korendyke, C.M., Brown, C.M., Myers, S., Mariska, J., Seely, J., Lang, J., Kent, B.J., Shaughnessy, B.M., Young, P.R., Simnett, G.M., Castelli, C.M., Mahmoud, S., Mapson-Menard, H., Probyn, B.J., Thomas, R.J., Davila, J., Dere, K., Windt, D., Shea, J., Hagood, R., Moye, R., Hara, H., Watanabe, T., Matsuzaki, K., Kosugi, T., Hansteen, V., Wikstol, Ø.: 2007, The EUV Imaging Spectrometer for Hinode. *Solar Phys.* **243**, 19. DOI. ADS.

Del Zanna, G.: 2009a, Benchmarking atomic data for astrophysics: Fe VII and other cool lines observed by Hinode EIS. *Astron. Astrophys.* **508**, 501. DOI. ADS.

Del Zanna, G.: 2009b, Benchmarking atomic data for astrophysics: Fe VIII EUV lines. *Astron. Astrophys.* **508**, 513. DOI. ADS.

Del Zanna, G.: 2010, Benchmarking atomic data for astrophysics: Fe xi. *Astron. Astrophys.* **514**, A41. DOI. ADS.

Del Zanna, G.: 2013a, A revised radiometric calibration for the Hinode/EIS instrument. *Astron. Astrophys.* **555**, A47. DOI. ADS.

Del Zanna, G.: 2013b, The multi-thermal emission in solar active regions. *Astron. Astrophys.* **558**, A73. DOI. ADS.

Del Zanna, G., O'Dwyer, B., Mason, H.E.: 2011, SDO AIA and Hinode EIS observations of "warm" loops. *Astron. Astrophys.* **535**, A46. DOI. ADS.

Del Zanna, G., Aulanier, G., Klein, K.-L., Török, T.: 2011, A single picture for solar coronal outflows and radio noise storms. *Astron. Astrophys.* **526**, A137. DOI. ADS.

Del Zanna, G., Dere, K.P., Young, P.R., Landi, E., Mason, H.E.: 2015, CHIANTI - An atomic database for emission lines. Version 8. *Astron. Astrophys.* **582**, A56. DOI. ADS.

Dere, K.P., Landi, E., Mason, H.E., Monsignori Fossi, B.C., Young, P.R.: 1997, CHIANTI - an atomic database for emission lines. *Astron. Astrophys. Suppl.* **125**, 149. DOI. ADS.

Doschek, G.A., Warren, H.P., Dennis, B.R., Reep, J.W., Caspi, A.: 2015, Flare Footpoint Regions and a Surge Observed by Hindode/EIS, RHESSI, and SDO/AIA. *Astrophys. J.* **813**, 32. DOI. ADS.

Feldman, U., Doschek, G.A., Behring, W.E., Phillips, K.J.H.: 1996, Electron Temperature, Emission Measure, and X-Ray Flux in A2 to X2 X-Ray Class Solar Flares. *Astrophys. J.* **460**, 1034. DOI. ADS.

Freeland, S.L., Handy, B.N.: 1998, Data Analysis with the SolarSoft System. *Solar Phys.* **182**, 497. DOI. ADS.

Garcia, H.A.: 1994, Temperature and emission measure from GOES soft X-ray measurements. *Solar Phys.* **154**, 275. DOI. ADS.

Glesener, L., Krucker, S., Lin, R.P.: 2012, Hard X-Ray Observations of a Jet and Accelerated Electrons in the Corona. *Astrophys. J.* **754**, 9. DOI. ADS.

Hong, J., Jiang, Y., Yang, J., Li, H., Xu, Z.: 2017, Minifilament Eruption as the Source of a Blowout Jet, C-class Flare, and Type-III Radio Burst. *Astrophys. J.* **835**, 35. DOI. ADS.

Hurford, G.J., Schmahl, E.J., Schwartz, R.A., Conway, A.J., Aschwanden, M.J., Csillaghy, A., Dennis, B.R., Johns-Krull, C., Krucker, S., Lin, R.P., McTiernan, J., Metcalf, T.R., Sato, J., Smith, D.M.: 2002, The RHESSI Imaging Concept. *Solar Phys.* **210**, 61. DOI. ADS.

Innes, D.E., Cameron, R.H., Solanki, S.K.: 2011, EUV jets, type III radio bursts and sunspot waves investigated using SDO/AIA observations. *Astron. Astrophys.* **531**, L13. DOI. ADS.

Klassen, A., Gómez-Herrero, R., Heber, B.: 2011, Electron Spikes, Type III Radio Bursts and EUV Jets on 22 February 2010. *Solar Phys.* **273**, 413. DOI. ADS.

Kosugi, T., Matsuzaki, K., Sakao, T., Shimizu, T., Sone, Y., Tachikawa, S., Hashimoto, T., Minesugi, K., Ohnishi, A., Yamada, T., Tsuneta, S., Hara, H., Ichimoto, K., Suematsu, Y.,

Shimojo, M., Watanabe, T., Shimada, S., Davis, J.M., Hill, L.D., Owens, J.K., Title, A.M., Culhane, J.L., Harra, L.K., Doschek, G.A., Golub, L.: 2007, The Hinode (Solar-B) Mission: An Overview. *Solar Phys.* **243**, 3. DOI. ADS.

Krucker, S., Saint-Hilaire, P., Christe, S., White, S.M., Chavier, A.D., Bale, S.D., Lin, R.P.: 2008, Coronal Hard X-Ray Emission Associated with Radio Type III Bursts. *Astrophys. J.* **681**, 644. DOI. ADS.

Krucker, S., Kontar, E.P., Christe, S., Glesener, L., Lin, R.P.: 2011, Electron Acceleration Associated with Solar Jets. *Astrophys. J.* **742**, 82. DOI. ADS.

Kundu, M.R., Raulin, J.P., Nitta, N., Hudson, H.S., Shimojo, M., Shibata, K., Raoult, A.: 1995, Detection of Nonthermal Radio Emission from Coronal X-Ray Jets. *Astrophys. J. Lett.* **447**, L135. DOI. ADS.

Lemen, J.R., Title, A.M., Akin, D.J., Boerner, P.F., Chou, C., Drake, J.F., Duncan, D.W., Edwards, C.G., Friedlaender, F.M., Heyman, G.F., Hurlburt, N.E., Katz, N.L., Kushner, G.D., Levay, M., Lindgren, R.W., Mathur, D.P., McFeaters, E.L., Mitchell, S., Rehse, R.A., Schrijver, C.J., Springer, L.A., Stern, R.A., Tarbell, T.D., Wuelser, J.-P., Wolfson, C.J., Yanari, C., Bookbinder, J.A., Cheimets, P.N., Caldwell, D., Deluca, E.E., Gates, R., Golub, L., Park, S., Podgorski, W.A., Bush, R.I., Scherrer, P.H., Gummin, M.A., Smith, P., Auker, G., Jerram, P., Pool, P., Soufli, R., Windt, D.L., Beardsley, S., Clapp, M., Lang, J., Waltham, N.: 2012, The Atmospheric Imaging Assembly (AIA) on the Solar Dynamics Observatory (SDO). *Solar Phys.* **275**, 17. DOI. ADS.

Li, X., Yang, S., Chen, H., Li, T., Zhang, J.: 2015, Trigger of a Blowout Jet in a Solar Coronal Mass Ejection Associated with a Flare. *Astrophys. J. Lett.* **814**, L13. DOI. ADS.

Lin, R.P., Dennis, B.R., Hurford, G.J., Smith, D.M., Zehnder, A., Harvey, P.R., Curtis, D.W., Pankow, D., Turin, P., Bester, M., Csillaghy, A., Lewis, M., Madden, N., van Beek, H.F., Appleby, M., Raudorf, T., McTiernan, J., Ramaty, R., Schmahl, E., Schwartz, R., Krucker, S., Abiad, R., Quinn, T., Berg, P., Hashii, M., Sterling, R., Jackson, R., Pratt, R., Campbell, R.D., Malone, D., Landis, D., Barrington-Leigh, C.P., Slassi-Sennou, S., Cork, C., Clark, D., Amato, D., Orwig, L., Boyle, R., Banks, I.S., Shirey, K., Tolbert, A.K., Zarro, D., Snow, F., Thomsen, K., Henneck, R., McHedlishvili, A., Ming, P., Fivian, M., Jordan, J., Wanner, R., Crubb, J., Preble, J., Matranga, M., Benz, A., Hudson, H., Canfield, R.C., Holman, G.D., Crannell, C., Kosugi, T., Emslie, A.G., Vilmer, N., Brown, J.C., Johns-Krull, C., Aschwanden, M., Metcalf, T., Conway, A.: 2002, The Reuven Ramaty High-Energy Solar Spectroscopic Imager (RHESSI). *Solar Phys.* **210**, 3. DOI. ADS.

Liu, J., Wang, Y., Shen, C., Liu, K., Pan, Z., Wang, S.: 2015, A Solar Coronal Jet Event Triggers a Coronal Mass Ejection. *Astrophys. J.* **813**, 115. DOI. ADS.

Liu, J., Wang, Y., Erdélyi, R., Liu, R., McIntosh, S.W., Gou, T., Chen, J., Liu, K., Liu, L., Pan, Z.: 2016, On the Magnetic and Energy Characteristics of Recurrent Homologous Jets from An Emerging Flux. *ArXiv e-prints.* ADS.

Liu, Y., Hoeksema, J.T., Scherrer, P.H., Schou, J., Couvidat, S., Bush, R.I., Duvall, T.L., Hayashi, K., Sun, X., Zhao, X.: 2012, Comparison of Line-of-Sight Magnetograms Taken by the Solar Dynamics Observatory/Helioseismic and Magnetic Imager and Solar and Heliospheric Observatory/Michelson Doppler Imager. *Solar Phys.* **279**, 295. DOI. ADS.

Madjarska, M.S.: 2011, Dynamics and plasma properties of an X-ray jet from SUMER, EIS, XRT, and EUVI A B simultaneous observations. *Astron. Astrophys.* **526**, A19. DOI. ADS.

Miao, Y.H., Liu, Y., Shen, Y.D., Elmhamdi, A., Kordi, A.S.: 2017, A coronal blowout jet associated with a double-CME and shock wave. *ArXiv e-prints.* ADS.

Mulay, S.M., Del Zanna, G., Mason, H.: 2017a, Cool and hot emission in a recurring active region jet. *Astron. Astrophys.* **606**, A4. DOI. ADS.

Mulay, S.M., Del Zanna, G., Mason, H.: 2017b, Temperature and density structure of a recurring active region jet. *Astron. Astrophys.* **598**, A11. DOI. ADS.

Mulay, S.M., Tripathi, D., Del Zanna, G., Mason, H.: 2016, Multiwavelength study of 20 jets that emanate from the periphery of active regions. *Astron. Astrophys.* **589**, A79. DOI. ADS.

Müller, D., Marsden, R.G., St. Cyr, O.C., Gilbert, H.R.: 2013, Solar Orbiter . Exploring the Sun-Heliosphere Connection. *Solar Phys.* **285**, 25. DOI. ADS.

Nitta, N.V., Reames, D.V., De Rosa, M.L., Liu, Y., Yashiro, S., Gopalswamy, N.: 2006, Solar Sources of Impulsive Solar Energetic Particle Events and Their Magnetic Field Connection to the Earth. *Astrophys. J.* **650**, 438. DOI. ADS.

Nitta, N.V., Mason, G.M., Wiedenbeck, M.E., Cohen, C.M.S., Krucker, S., Hannah, I.G., Shimojo, M., Shibata, K.: 2008, Coronal Jet Observed by Hinode as the Source of a ^{3}He-rich Solar Energetic Particle Event. *Astrophys. J. Lett.* **675**, L125. DOI. ADS.

Nitta, N.V., Mason, G.M., Wang, L., Cohen, C.M.S., Wiedenbeck, M.E.: 2015, Solar Sources of ^{3}He-rich Solar Energetic Particle Events in Solar Cycle 24. *Astrophys. J.* **806**, 235. DOI. ADS.

O'Dwyer, B., Del Zanna, G., Mason, H.E., Weber, M.A., Tripathi, D.: 2010, SDO/AIA response to coronal hole, quiet Sun, active region, and flare plasma. *Astron. Astrophys.* **521**, A21. DOI. ADS.

Ogawara, Y., Takano, T., Kato, T., Kosugi, T., Tsuneta, S., Watanabe, T., Kondo, I., Uchida, Y.: 1991, The SOLAR-A Mission - An Overview. *Solar Phys.* **136**, 1. DOI. ADS.

Panesar, N.K., Sterling, A.C., Moore, R.L.: 2016, Homologous Jet-driven Coronal Mass Ejections from Solar Active Region 12192. *Astrophys. J. Lett.* **822**, L23. DOI. ADS.

Pesnell, W.D., Thompson, B.J., Chamberlin, P.C.: 2012, The Solar Dynamics Observatory (SDO). *Solar Phys.* **275**, 3. DOI. ADS.

Pick, M., Mason, G.M., Wang, Y.-M., Tan, C., Wang, L.: 2006, Solar Source Regions for ^{3}He-rich Solar Energetic Particle Events Identified Using Imaging Radio, Optical, and Energetic Particle Observations. *Astrophys. J.* **648**, 1247. DOI. ADS.

Polito, V., Reep, J.W., Reeves, K.K., Simões, P.J.A., Dudík, J., Del Zanna, G., Mason, H.E., Golub, L.: 2016, Simultaneous IRIS and Hinode/EIS Observations and Modelling of the 2014 October 27 X2.0 Class Flare. *Astrophys. J.* **816**, 89. DOI. ADS.

Raulin, J.P., Kundu, M.R., Hudson, H.S., Nitta, N., Raoult, A.: 1996, Metric Type III bursts associated with soft X-ray jets. *Astron. Astrophys.* **306**, 299. ADS.

Scherrer, P.H., Schou, J., Bush, R.I., Kosovichev, A.G., Bogart, R.S., Hoeksema, J.T., Liu, Y., Duvall, T.L., Zhao, J., Title, A.M., Schrijver, C.J., Tarbell, T.D., Tomczyk, S.: 2012, The Helioseismic and Magnetic Imager (HMI) Investigation for the Solar Dynamics Observatory (SDO). *Solar Phys.* **275**, 207. DOI. ADS.

Schou, J., Scherrer, P.H., Bush, R.I., Wachter, R., Couvidat, S., Rabello-Soares, M.C., Bogart, R.S., Hoeksema, J.T., Liu, Y., Duvall, T.L., Akin, D.J., Allard, B.A., Miles, J.W., Rairden, R., Shine, R.A., Tarbell, T.D., Title, A.M., Wolfson, C.J., Elmore, D.F., Norton, A.A., Tomczyk, S.: 2012, Design and Ground Calibration of the Helioseismic and Magnetic Imager (HMI) Instrument on the Solar Dynamics Observatory (SDO). *Solar Phys.* **275**, 229. DOI. ADS.

Sterling, A.C., Moore, R.L., Panesar, N.K.: 2018, Magnetic Flux Cancelation as the Buildup and Trigger Mechanism for CME-Producing Eruptions in two Small Active Regions. *ArXiv e-prints*. ADS.

Thomas, R.J., Crannell, C.J., Starr, R.: 1985, Expressions to determine temperatures and emission measures for solar X-ray events from GOES measurements. *Solar Phys.* **95**, 323. DOI. ADS.

Wang, Y.-M., Pick, M., Mason, G.M.: 2006, Coronal Holes, Jets, and the Origin of ^{3}He-rich Particle Events. *Astrophys. J.* **639**, 495. DOI. ADS.

White, S.M., Thomas, R.J., Schwartz, R.A.: 2005, Updated Expressions for Determining Temperatures and Emission Measures from Goes Soft X-Ray Measurements. *Solar Phys.* **227**, 231. DOI. ADS.

Zhang, Q.M., Ji, H.S.: 2014, A swirling flare-related EUV jet. *Astron. Astrophys.* **561**, A134. DOI. ADS.